Nanoscale

REVIEW

View Article Online
View Journal | View Issue

Cite this: *Nanoscale*, 2022, **14**, 13890

A guide to the design of magnetic particle imaging tracers for biomedical applications

H. T. Kim Duong,[a] Ashkan Abdibastami,[a] Lucy Gloag, *[a] Liam Barrera,[a] J. Justin Gooding *[a,b] and Richard D. Tilley *[a,c]

Received 6th April 2022,
Accepted 11th August 2022

DOI: 10.1039/d2nr01897g

rsc.li/nanoscale

Magnetic Particle Imaging (MPI) is a novel and emerging non-invasive technique that promises to deliver high quality images, no radiation, high depth penetration and nearly no background from tissues. Signal intensity and spatial resolution in MPI are heavily dependent on the properties of tracers. Hence the selection of these nanoparticles for various applications in MPI must be carefully considered to achieve optimum results. In this review, we will provide an overview of the principle of MPI and the key criteria that are required for tracers in order to generate the best signals. Nanoparticle materials such as magnetite, metal ferrites, maghemite, zero valent iron@iron oxide core@shell, iron carbide and iron–cobalt alloy nanoparticles will be discussed as well as their synthetic pathways. Since surface modifications play an important role in enabling the use of these tracers for biomedical applications, coating options including the transfer from organic to inorganic media will also be discussed. Finally, we will discuss different biomedical applications and provide our insights into the most suitable tracer for each of these applications.

1. Introduction

Magnetic particle imaging (MPI) is an emerging non-invasive imaging modality that uses superparamagnetic magnetic nanoparticles (MNPs) as tracers.[1–6] MPI has attracted great attention owing to its high sensitivity, spatial resolution, and strong signal intensities without a background signal from tissue.[5,7,8] MPI is a tracer-based imaging modality where high quality MNPs are required. Superparamagnetic iron oxide MNPs (SPIONs) are the most commonly used tracers.[1–6] Many researchers around the world are exploring the synthesis and optimisation of MNPs that can deliver exceptional signal intensities and resolution in MPI for a range of applications. These applications include *in vivo* imaging,[9–11] cancer cells targeting,[4,5,12,13] cellular tracking,[8,14–17] and hyperthermia therapy.[18–20] Importantly, the MNP tracers required for these applications can be different and may need to be further modified or tailored for each specific application.

[a]*School of Chemistry, UNSW Sydney, NSW 2052, Australia. E-mail: r.tilley@unsw.edu.au*
[b]*Australian Centre for NanoMedicine, University of New South Wales, NSW 2052, Australia*
[c]*Electron Microscope Unit, Mark Wainwright Analytical Centre, University of New South Wales, NSW 2052, Australia*

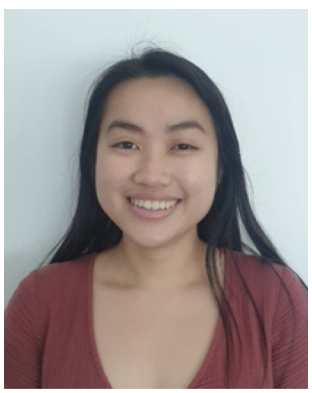

H. T. Kim Duong

Hong Thien Kim Duong is a PhD candidate in the School of Chemistry at the University of New South Wales (UNSW) under the supervision of Prof. Richard Tilley and Prof. Justin Gooding. She graduated with a B. AdvSc. (Hons) at UNSW. Her current research focuses on the synthesis and functionalisation of magnetic nanoparticles for Magnetic Particle Imaging (MPI).

Lucy Gloag

Lucy Gloag is a postdoctoral research fellow in the School of Chemistry at the University of New South Wales (UNSW). She graduated with a B.Sc. (Hons) degree from the Victoria University of Wellington and a Ph.D. degree from UNSW. Her current research focuses on shape control of metallic nanocrystals for catalysis and biomedicine applications.

MNPs such as iron or iron oxide MNPs show immense promise in biomedical applications, especially MPI, due to their non-toxicity and high magnetic performance. Since the MNP materials are the source of MPI signal generation, the selection of such material needs to be carefully considered in order to achieve the best results. Materials such as magnetite, metal ferrites, maghemite, zero valent iron@iron oxide core@-shell, iron carbide and iron–cobalt alloy NPs show the most promise as potential tracers for MPI. In this paper, we will discuss each MNP material at length and their synthetic routes as well as providing our insights on what would be the "best" MNP material for MPI. We also focus on different surface modifications of MNPs and the suitability of each type of coating for different biomedical applications.

2. Magnetic nanoparticles (MNPs)

Magnetic nanoparticles (MNPs) have shown great potential in a broad range of biomedical applications ranging from hyperthermia for cancer treatment,[18–20] drug delivery guided by magnetic fields,[21] highly sensitive biosensors,[22–24] and biomedical imaging such as Magnetic Particle Imaging (MPI) and Magnetic Resonance Imaging (MRI).[2,20] Iron oxide is the most commonly used material for biomedical applications due to the relative ease of synthesis and stability at room temperature. Additionally, SPIONs have been clinically approved to be used to treat anaemia.[2] Due to their favourable magnetic properties, magnetite and maghemite crystal phases of iron oxide are the most widely used as contrast agents and tracers in biomedical imaging.

Since the signals generated in MPI are strongly dependent on the magnetic properties of the MNPs used as MPI tracers, we need to be mindful of the key criteria to achieve the best signals. These criteria are superparamagnetism, short magnetic relaxation time and high saturation magnetisation (M_{sat}) which are strongly affected by the size of MNPs. We will discuss each of these in turn in the following section.

3. Important factors that affect the magnetic properties in generating MPI signals

In MPI, a time-varying magnetic field is scanned continuously over the region of interest in all three dimensions.[5,7,10,25] This causes the electron spins from the MNPs to align with the magnetic field. When they are in the field free region (FFR), where there is no magnetic field strength, complete magnetic relaxation is allowed causing the electron spins to instantaneously flip.[5,7,10,25] This magnetic phenomenon is illustrated in Fig. 1a. This change in magnetic spin induces signals that will be converted into tomographic images of the area of interest.[5,7,10,25] Therefore, properties such as superparamagnetism, magnetic relaxation, and saturation magnetisation are highly important for the generation of good MPI signals.

3.1. Superparamagnetism

Superparamagnetic MNPs are highly desired for the synthesis of the "ideal" MPI tracers as they have negligible coercivity and magnetic remanence.[26] Coercivity (H_c) is defined as the magnetic field strength needed to bring the magnetisation of the material back to zero; and magnetic remanence is defined as the magnetisation left behind from magnetic materials after an external magnetic field is removed. With negligible coercivity, superparamagnetic NPs can relax instantly upon the removal of the external field and hence can achieve fast magnetic relaxation to achieve sharp and high-resolution images, MNPs with superparamagnetic behaviour are essential for the synthesis of good tracers. Additionally, apart from lower image quality, permanently magnetic MNPs can cause aggregation as a result of an increase in coercivity value.[27]

3.2. Short magnetic relaxation

The mode of relaxation is one of the most important factors that affects the spatial resolution of MPI. This is because a shorter relaxation generates a sharper MPI signal and hence a

Justin Gooding

J. Justin Gooding graduated with a B.Sc. (Hons) degree from Melbourne University,and completed a Ph.D. degree at the University of Oxford and postdoctoral training at the Institute of Biotechnology in Cambridge University. After starting as a Research Fellow at the University of New South Wales, he gained Professorship in 2006. He is an ARC Australian Laureate Fellow and codirector of the Australian Centre for NanoMedicine. He leads a research team in surface modification and nanotechnology for biosensors and biomaterials.

Richard D. Tilley

Richard D. Tilley is the Director of Electron Microscope Unit and a Professor in the School of Chemistry at the University of New South Wales (UNSW). He graduated with a Masters of Chemistry from Oxford University and then completed his Ph.D. degree at the University of Cambridge, after which he was a Postdoctoral Fellow at the Toshiba Basic R&D Center, Tokyo. He leads a research team focused on the solution synthesis of nanocrystals for catalysis and biomedical imaging

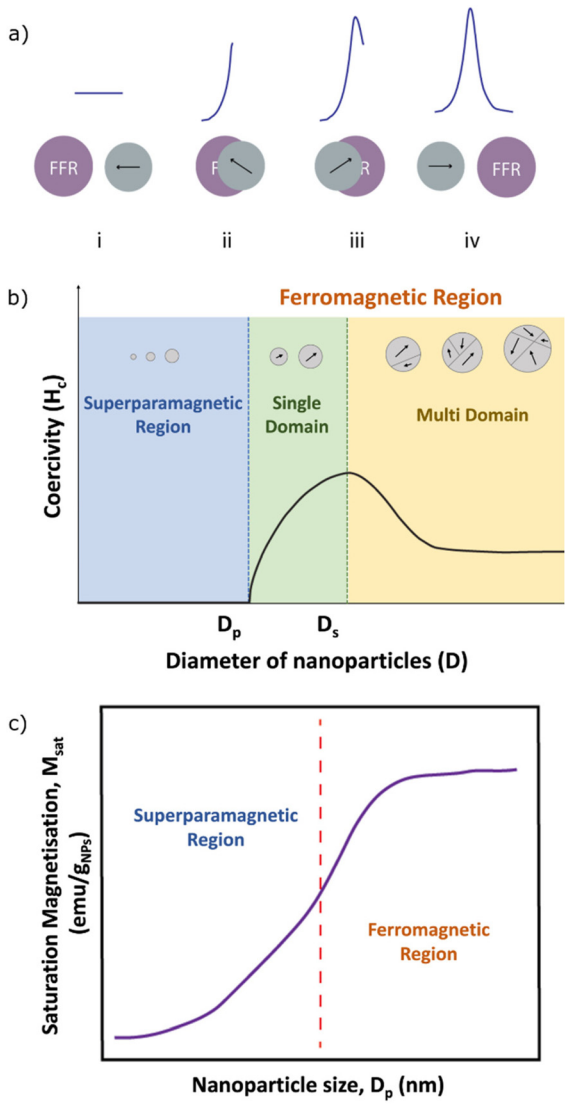

Fig. 1 (a) Illustration of how signals are generated in MPI. The magnetic spins within the MNP align with the magnetic field as the FFR approaches, resulting in no signal (I). As the FFR passes over the MNP, the magnetic spin begins to flip and the change in spin direction is translated to an increase in signal (II). The signal peaks where the FFR is directly over the MNP (III) and then the spin points in the opposite direction to produce a localised MPI signal (IV) (b) Coercivity *versus* diameter of MNPs. No coercivity is produced below D_p in the superparamagnetic region. Coercivity then increases as the MNP size increases until D_s where multiple magnetic domains are produced and the coercivity is lowered. (c) Saturation magnetisation increases with MNP size over the superparamagnetic region and reaches a plateau in the ferromagnetic region.

higher resolution image. There are two types of magnetic relaxation, which are Brownian and Néel relaxation. Brownian relaxation is due to the rotation of the whole particle entity in the carrier fluid and typically occurs on the microsecond timescale.[28,29] Néel relaxation is caused by the realignment of the internal magnetic spins inside the NPs after the removal of an external field and can occur for nanoseconds for superparamagnetic NPs to years for ferromagnetic particles.[28,29] Since MPI signals are generated from the relaxation of the magnetic spins at the FFR, producing MNPs that are superparamagnetic with short Néel relaxation is of high importance for the synthesis of MPI tracers with high spatial resolution.

3.3. Size of MNPs

Superparamagnetism is highly size dependent and hence MNP sizes must be carefully controlled to achieve excellent performance in MPI. As illustrated in Fig. 1b, the coercivity remains zero in the superparamagnetic region (*i.e.*, MNPs with sizes less than the critical diameter of the particle (D_p) and gradually increases when the MNPs are larger than this critical size and enter the ferromagnetic region. The critical size limit D_p (usually nanometres size range) varies for different materials and hence must be determined for the synthesis of superparamagnetic NPs. The coercivity is seen to reach maximum at a size where the magnetic domains within NPs change from single to multi-domains, denoted D_S in Fig. 1.

The importance of MNP size was clearly demonstrated in a study conducted by Krishnan and co-workers where they investigated different sizes of magnetite.[27] The results show that only MNPs that are close to the critical size (D_p of 25 nm for ultrafine magnetically ordered particles) and single crystalline displayed adequate signal strength and resolution for MPI.[27,30] Plus, any MNP sizes that are larger than 25.3 nm show minimal to no enhancement in signal compared to smaller MNPs due to ferromagnetic (permanent magnetic) behaviour. Therefore, it is critical to carefully control the size of the MNPs so it can maintain its superparamagnetic behaviour to achieve the best MPI signal.

MNP size also dictates the size of the internal magnetic spin that determines the M_{sat} and signal intensity, as shown in Fig. 1c. For single domain MNPs, M_{sat} increases linearly to D_p in both the superparamagnetic and ferromagnetic regimes. As size increases further in the ferromagnetic region, and the MNPs are forced to become multi-domain, the size of the magnetic spins cannot increase further and M_{sat} plateaus. Consequently, high M_{sat} values lower the limit of detection as fewer MNPs are needed to generate the same amount of MPI signal. Furthermore, higher signal intensity can also provide sharper and clearer images hence ultimately increase the quality of diagnosis. In theory, the larger the MNP the more magnetic domains it has, and the higher the saturation magnetisation (see Fig. 1b).[31,32] The ideal synthesis for good MPI tracers is one that achieves single domain MNPs that are close to the critical size limit. Each magnetic material has a different critical size limit and so the optimal size differs for each material. This ensures the highest M_{sat} while still maintaining their superparamagnetism. This further emphasises the importance of precise size control and single crystallinity when synthesising MPI tracers so that images can be generated with both high spatial resolution and high signal intensity.[22]

Controlling size distribution during synthesis of MNPs is important. MNPs with a narrow size distribution, or monodispersity, deliver excellent and consistent image quality.[33] When

the size distribution is large, there will be a range of MNPs that are different in magnetic properties. For example, larger ferromagnetic NPs with broad signals, and smaller MNPs with low intensity signals. Overall, the quality of MPI signal is significantly affected by variance in magnetic properties of MPI tracers.[34] Therefore, it is important to synthesise monodispersed MNPs at the critical size to achieve exceptional and consistent image quality in MPI.

4. MNP design

In this section, we highlight recent progress in the design of MNPs with optimised magnetic properties for MPI. Composition, nanostructure, crystallinity, size, monodispersity, and morphology of MNPs are considered to be the most crucial factors determining magnetic properties of MPI tracers.[11] By controlling these structural features, MNPs can be tuned to show higher M_{sat} and faster relaxation in order to provide higher signal intensity, spatial resolution and sensitivity.

4.1. Material choice for MNPs

Different MNP compositions such as metallic oxides, core–shell, ferrite NPs, and metal alloys have a range of interesting and unique magnetic properties.[35–37] The material should be chosen based on the desired properties, such as size requirement, additional chemical properties or oxidation resistance (Fig. 2).

4.1.1. Iron oxide nanoparticles. Iron oxides display superparamagnetism, biocompatibility, ease of preparation and lower toxicity.[2,36,38–44] For these reasons, SPIONs have garnered significant attention as promising candidates for designing MPI tracers.[4,45]

Several commercialised tracers that use SPIONs such as ferucarbotran (a.k.a. Resovist from Bayer Schering, and Vivotrax from Magnetic Insight Inc.), Synomag®-D and Perimag® (from Micromod Partikeltechnologie GmbH) have been already reported to generate good MPI signals.[8,46–52] However, commercial tracers have been reported to have broad size distributions, and aggregated clusters, which lowers their spatial resolution and their *in vivo* circulation time.[47,50,51,53] For example, Resovist has been designed on the basis of polycrystalline iron oxide MNPs consisting of multiple single crystals coated with carboxydextran with a hydrodynamic size of more than 60 nm in diameter.[54,55] When a weak external field is applied to polycrystalline MNPs, the individual magnetic moment vectors cannot linearly sum due to the availability of antiphase boundaries, resulting in a lower M_{sat} value.[25] Additionally, only MNPs with a diameter of about 30 nm play a significant role in the overall signal generation according to Langevin-theory, which means that only 3% of the total iron mass of the Resovist® solution contributes to the MPI signal.[7] The presence of a large fraction of nanoparticle clusters also adversely affects the blood circulation time of these nanoparticles in physiological environment (*i.e.* 3.9 min to 5.8 min in blood).[47,55–57]

A new versatile approach based on designing monodisperse single crystal SPIONs is needed to achieve both long circulation time and high signal intensity for MPI-tailored tracers. In the following paragraphs, we will be focusing on different MNP materials and provide our insights into the advantages and disadvantages of each, and which would be perceived as "best" MNP material.

Of all iron oxide crystal phases, magnetite has been the most studied MNP material for MPI tracers due to the ease of controlled synthesis of single crystalline, high M_{sat} value and high reproducibility.[2,58,59] The magnetic moments of magnetite can also be easily saturated in the magnetic fields of just tens of mT in biological environments, leading to a strong magnetisation response for non-invasive MPI application.[60] In terms of MPI performance, spatial resolution, and signal intensity, monodisperse magnetite tracers have also shown great promise. For instance, MPI performance of magnetite MNPs, studied by Krishnan and co-workers, showed 2-fold enhancement in signal per unit mass as well as 20% better spatial resolution compared to commercial agents (Fig. 2a).[6] Moreover, as compared to Resovist and mixed-phase NPs, magnetite has the narrowest full width at half maximum (FWHM) of the differential susceptibility (dm/dH) in magnetic particle spectroscopy (MPS), indicating higher potential to improve MPI spatial resolution.[59] Magnetite also displays decreased saturation field and increased susceptibility in vibrating sample magnetometry (VSM), which demonstrates the desirable magnetic properties for MPI application.[59]

Metal ferrites (or doped magnetite NPs) have gained a lot of research interests owing to their high saturation magnetisation, ease of preparation, high electrical resistivity and good conductivity.[62–65] They are classified as either "soft", "semi-hard" or "hard" depending on their magnetic properties. Soft ferrites have low coercivity while hard ferrites have high coercivity. For biomedical imaging, soft ferrites (with non-permanent magnetism) are the preferred material.[66] Monodisperse doped magnetite NPs have a general formula of $M_xFe_{3-x}O_4$ where M designates transition-metals, such as Mn, Zn, Ni and Co. Different metal doping can have different effects on the properties of MNP tracers (Fig. 2b).

4.1.2. Zinc doped ferrites ($Zn_xFe_{3-x}O_4$). Doping magnetite with zinc can effectively increase the M_{sat} of the bulk materials. The crystal structure of magnetite possesses anti-parallel magnetic spins in the tetrahedral sites which consequently lower the net M_{sat} of the material. However, when doping magnetite with zinc, the anti-parallel Fe^{3+} magnetic spins can be replaced by the diamagnetic Zn^{2+} increase the M_{sat} value. According to the recent study of the MPI performance of Zn-doped magnetite NPs by Bauer *et al.*, it was demonstrated that doping Zn up to 13% into a magnetite structure can lead to enhancement of the signal-to-noise ratio (SNR) due to a significant increase in M_{sat} values from 101.2–107.3 emu g_{Fe}^{-1} to 125.7–130.4 emu g_{Fe}^{-1}. The best MPI signal was observed for spherical Zn-doped magnetite NPs, which displayed a symmetric point spread function (PSF) as well as higher SNR.[19] In another recent study conducted by Jiang *et al.*, carbon supported metal

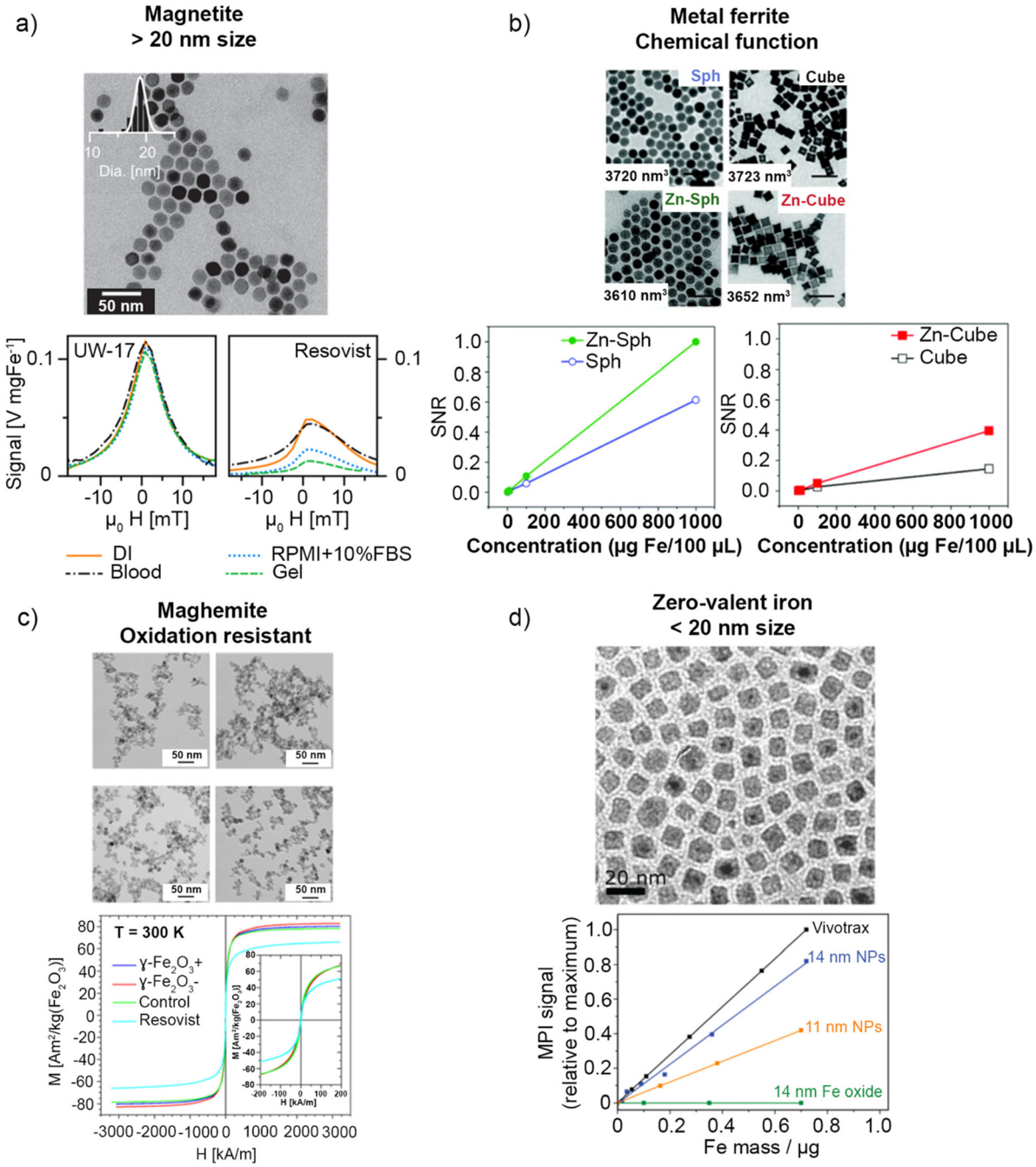

Fig. 2 Comparison of different types of magnetic nanoparticles for MPI based on the desired properties and their performance. (a) TEM images of >15 nm magnetite NPs with enhanced MPI signal intensity compared to Resovist.[6] This figure has been reproduced from ref. 6 with permission from Biomaterials, copyright 2022. (b) TEM images of spherical and cubic zinc ferrite NPs showing enhanced MPI signal for Zn doped ferrites compared to non-doped magnetite, as well as higher MPI signals for spheres compared to cubes.[19] This figure has been reproduced from ref. 19 with permission from Nanoscale, copyright 2022. (c) TEM images of maghemite NPs and the hysteresis curve of uncoated anionic and cationic Fe_2O_3 at room temperature, showing higher M_{sat} than Resovist.[61] This figure has been reproduced from ref. 61 with permission from Journal of Nanoparticle Research, copyright 2022. (d) TEM images of <15 nm zero valent Fe@Fe_3O_4 NPs with higher MPI signal relative to iron oxide of the same size and similar MPI performance to larger VivoTrax.[26] This figure has been reproduced from ref. 26 with permission from Chemical Communications, copyright 2022.

ion doped MFe_2O_4/C (M = Mn, Co, or Zn) and γ-Fe_2O_3/C were synthesised through the pyrolysis of MIL-88A at 450 °C and then coated with polydopamine (PDA) to be water-dispersible. Although the VSM showed that $ZnFe_2O_4$/C had lower M_{sat} (32.06 emu g^{-1}) than that of γ-Fe_2O_3/C (48.01 emu g^{-1}) and $MnFe_2O_4$/C (50.07 emu g^{-1}), *in vitro* MPI measurements

demonstrated that $ZnFe_2O_4$/C@PDA can increase the MPI signal intensity (*i.e.*, 1787.7) up to 2.4 and 4.7 times greater than that of γ-Fe_2O_3/C@PDA (*i.e.*, 729.32) and commercial Vivotrax (*i.e.*, 383.2). It was reported that the free rotation of NPs can be limited in the carbon supported SPIONs, leading to an increase in Néel relaxation and improved MPI signal intensity.[48] The *in vivo* investigation on ECA-109 tumour nude mice also showed that $ZnFe_2O_4$/C@PDA had the highest MPI signal intensity (*i.e.*, 567.98) at 12 h, which was 4.5 and 7.5 times higher than γ-Fe_2O_3/C@PDA and $ZnFe_2O_4$, respectively (Fig. 3), indicating its high potential for enhancing the MPI performance in the tumours *in vivo*. In addition, $ZnFe_2O_4$/C@PDA was biocompatible in both *in vitro* and *in vivo* conditions.[48]

4.1.3. Manganese doped ferrites ($Mn_xFe_{3-x}O_4$). Manganese doped magnetite MNPs are another commonly used material for biological applications due to their non-toxicity and high M_{sat}. Manganese ferrite ($Mn_xFe_{3-x}O_4$) has Mn^{2+} cations can occupy both octahedral and tetrahedral sites in the magnetite crystal structure, replacing both parallel and anti-parallel spins.[67] According to the electron spin configurations, the magnetic spins of $MnFe_2O_4$ is about $5\mu_B$, leading to a high magnetic susceptibility.[67,68] The M_{sat} value of $MnFe_2O_4$ NPs (12 nm) was previously studied by Lee *et al.* using SQUID magnetometry and reported to be around 110 emu g^{-1} of magnetic atoms.[67] They are also shown to possess a superparamagnetic nature for MNPs of size that is smaller than 42 nm.[69] Manganese ferrite NPs have also been widely used as nanocarriers for antitumour drugs due to their high biocompatibility and strong magnetic susceptibility.[70–72] Studies have found that manganese ferrite MNPs show slight toxicity towards HeLa cells and so have potential for use in magnetoliposomes and drug delivery.[71] Furthermore, a study conducted by Miao *et al.* showed an improved biodistribution of these MNPs with increasing concentration of doped manganese.[73] Therefore, manganese ferrite NPs show great potential as MPI tracers for drug delivery and cancer cell targeting applications.

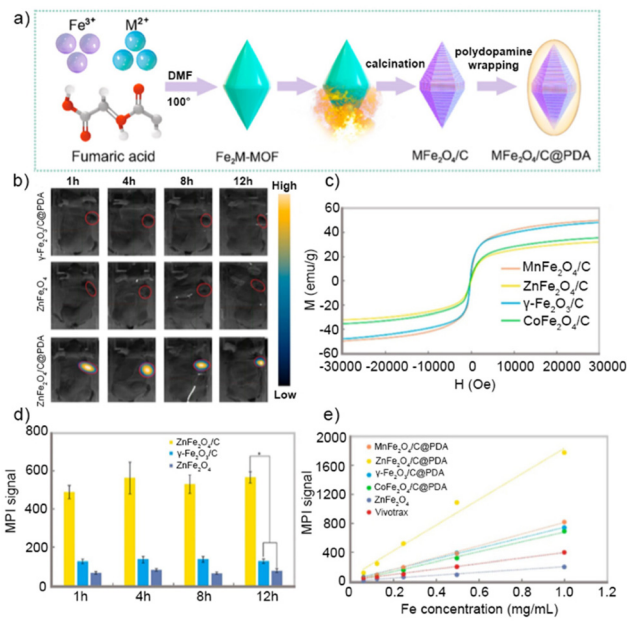

Fig. 3 (a) Schematic diagram of the synthesis of MFe_2O_4/C@PDA, (b) MPI images of NP distribution in ECA-109 tumour mouse model (n = 3). *In vivo* dynamic MPI of mice intratumorally injected with $ZnFe_2O_4$, γ-Fe_2O_3/C@PDA, and $ZnFe_2O_4$/C@PDA. (The tumour was labelled by a red circle.) Hysteresis curve showing saturation magnetisation of $MnFe_2O_4$/C, $ZnFe_2O_4$/C, γ-Fe_2O_4/C and $CoFe_2O_4$/C NPs, (d) MPI signal calculation and comparison between different groups and (e) MPI signal intensity for $MnFe_2O_4$/C@PDA, $ZnFe_2O_4$/C@PDA, γ-Fe_2O_4/C@PDA, $CoFe_2O_4$/C@PDA, $ZnFe_2O_4$ and Vivotrax.[48] This figure has been reproduced from ref. 48 with permission from Nano Letters, copyright 2022.

4.1.4. Cobalt doped ferrites ($Co_xFe_{3-x}O_4$). In contrast to zinc and manganese, cobalt is a dopant that is also magnetic and so has many interesting properties that can improve the applications of doped magnetite. In cobalt ferrite, the Co^{2+} cations prefer to occupy octahedral sites in the magnetite crystal so that tetrahedral sites are occupied by Fe^{3+} and octahedral sites are occupied by both Co^{2+} and Fe^{3+}.[67] However, the occupation of octahedral sites with a less magnetic cation results in a decrease in the parallel magnetic moments and in turn a decrease in the total magnetic response.[25] Studies have shown that magnetic spins of $CoFe_2O_4$ (12 nm) is about $3\mu_B$ and M_{sat} value is around 99 emu g^{-1} which is lower than pure magnetite (101 emu g^{-1}) of the same size.[67,68] Although, possessing a slightly lower M_{sat} than pure magnetite, cobalt ferrite is classified as a semi-hard ferrite, meaning that it has high coercivity (*i.e.*, a wider hysteresis loop).

High coercivity is an important property for magnetic hyperthermia applications, which is a therapeutic method for cancer treatment using heat. Cobalt ferrite nanoparticles have higher magnetic heating performance than magnetite and hence display great potential to be used as MPI tracers for hyperthermia application. As seen in Fig. 4, the amount of Co dopant impacts the coercivity of the material:[74] The higher the amount of Co content, the larger the coercive fields and hence the better the heating performance. However, when the coercivity becomes too large, this can adversely affect the specific heating power of the nanoparticles and decrease the effectiveness as hyperthermia agents. Therefore, the content of Co dopant must be carefully adjusted in order to achieve excellent heating performance in magnetic hyperthermia.

4.1.5. Nickel doped ferrites ($Ni_xFe_{3-x}O_4$). Nickel ferrite (with general formula of $Ni_xFe_{3-x}O_4$) also uses a less magnetic dopant atom. Similar to cobalt ferrite, nickel ferrites have T_h sites occupied by Fe^{3+} and O_h sites occupied by Ni^{2+} and Fe^{3+} atoms. However, nickel ferrites are classified as a soft ferrite, with low coercivity, due to the weaker magnetism of Ni atoms. The magnetic spin and mass magnetisation value of nickel ferrite NPs (12 nm) have been reported to be about $2\mu_B$ and 85 emu g^{-1}.[67] In one study, Irfan *et al.*, synthesised Ni-ferrites ($NiFe_2O_4$) by hydrothermal process, followed by coating with polyacrylic acid (PAA). The $NiFe_2O_4$@PAA demonstrated a minimum relaxation time of 3.10 μs and high spatial resolution of 7.75 mT, which makes it a promising candidate for MPI tracers compared to Vivotrax and Perimag.[75]

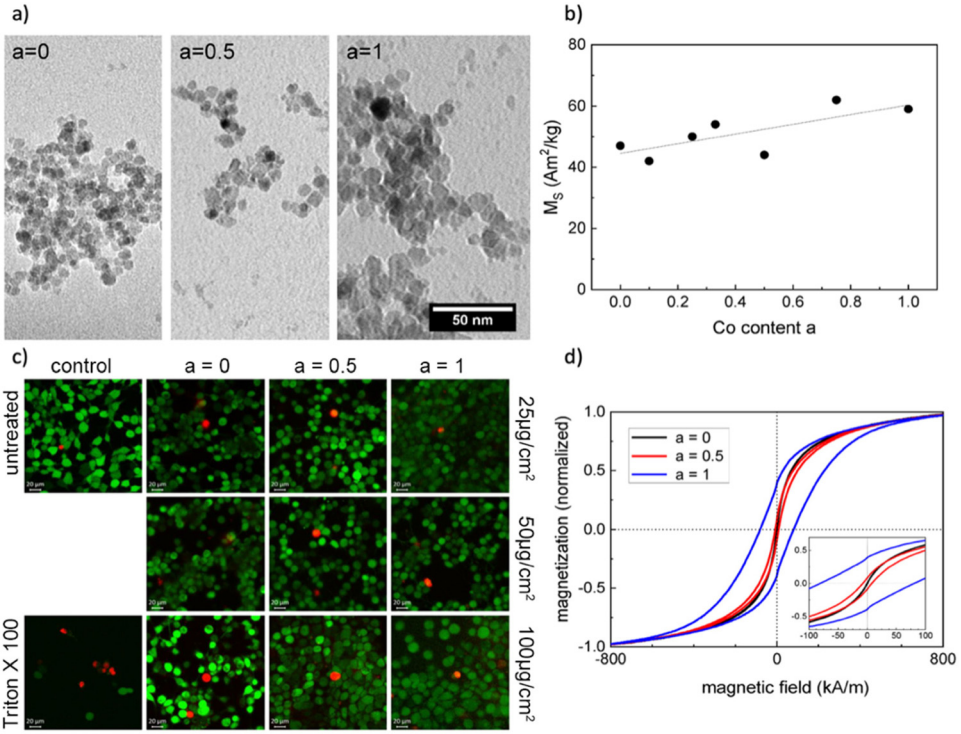

Fig. 4 (a) TEM images of cobalt ferrite nanoparticles at different Co content (a = 0, 0.5 and 1), (b) plot showing saturation magnetisation (M_s) of nanoparticles at various cobalt content, (c) cell viability of cobalt ferrite nanoparticles using fluorescent staining at different Co content (a = 0, 0.5 and 1) for 24 h and (c) normalised hysteresis loops of pure magnetite (a = 0) and particles with a Co content of 12.5% (a = 0.5) as well as 25% (a = 1) recorded at room temperature confirm a significant increase in the coercivity for increasing Co content of the particles. The inset shows the hysteresis curves at low magnetic field strengths.[74] This figure has been reproduced from ref. 74 with permission from Nanomaterials, copyright 2022.

4.1.6. Maghemite (γ-Fe_2O_3). Maghemite with the chemical formula γ-Fe_2O_3 is another crystal phase of iron oxide MNPs that has only fully oxidised Fe^{3+} ions in the crystal lattice. It is attractive for MPI tracers because it has high M_{sat} and is low toxicity. Since maghemite is metastable, its transformation to thermodynamically stable phases (hematite) is very slow.[43,76] This is important because the more strongly magnetic magnetite phase has been reported to readily degrade to non-magnetic hematite *in vivo*.[77] Owing to its acceptable magnetic properties as well as good relative stability, maghemite can potentially be used as a platform for designing the MNP MPI tracers for *in vivo* applications (Fig. 2c).

Recently, the MPI signal quality of monodisperse spherical maghemite MNPs was investigated by evaluation of the SNR and signal displacement parameters. Herynek *et al.*, demonstrated that anionic monodisperse γ-Fe_2O_3 MNPs with an average diameter of 8.7 nm coated by methacrylamide-based polymer with hydrodynamic size of 109.1 ± 0.1 nm can provide a higher signal with a lower dispersion than commercial tracers.[61] The magnetometry analysis of the maghemite MNPs at room temperature (300 K) demonstrated that both anionic and cationic MNPs display anhysteretic magnetisation curves (with low coercivity) as well as faster Néel relaxation and narrower distribution of blocking temperatures. The results shows that the M_{sat} of anionic and cationic maghemite MNPs (82.5 and 79.9 $Am^2\ kg^{-1}$, respectively) was significantly higher than that of Resovist®. In terms of MPI signal quality, coated anionic MNPs demonstrated SNR and signal dispersion identical to or lower than Resovist®.[61] These results show that maghemite is a promising material for MPI tracers but further work is needed to create MNPs that generate improved signals.

4.1.7. Zero valent iron or iron@iron oxide shell (Fe@Fe_3O_4). As zero valent iron has the highest M_{sat} value, α-iron has a great potential to become a promising candidate for designing the MNP of high performance MPI tracers. In addition, recent studies have shown that iron NPs have a good stability in physiological environments.[78] At the nanoscale level where superparamagnetic regime becomes dominant,[79] zero valent iron NPs still generate much higher M_{sat} value (176 emu g^{-1}) than SPIONs whose M_{sat} typically ranges from 20 to 80 emu g^{-1}.[26,80–82] This means that nanoparticles made of zero valent iron can generate MPI signal at smaller sizes than iron oxides (Fig. 2d) However, the high reactivity of iron towards oxygen leads to the formation of an unavoidable oxide shell.[26,83,84] The thickness of the oxide shell can range from 0.7 nm for ultrafine iron cores (2 nm) to a few nanometers (3–4 nm) for 8–15 nm cores.[26,78,84,85] For example, by slow thermal decomposition of $Fe(C_5H_5)(C_6H_7)$ in oleylamine (OLA) and mesitylene under a hydrogen gas atmosphere, Gloag *et al.*, synthesised a cube-shaped zero valent iron core–iron oxide shell structure with a core size of 8 nm and shell size of 3 nm followed by coating with polyethylene glycol (PEG) that

induced M_{sat} values 3 times higher than typical SPIONs of the same size (166 emu g_{Fe}^{-1}). Furthermore, 1.8 mm spatial resolution and 80% signal intensity of commercial VivoTrax were successfully achieved.[26] This higher magnetisation result was in consistent with previous studies conducted by Cheong *et al.*, who synthesised single crystal iron core MNPs *via* thermal decomposition of organometallic sandwich compound.[80,84] In addition, PEG–coated zero valent iron core–iron oxide shell structure was demonstrated to have no significant toxicity *in vitro* due to its excellent cell viability result (*i.e.*, >85%).[26] Furthermore, the zero valent iron core–iron oxide shell NPs was also demonstrated to be able to induce tumour cell ferroptosis and immunogenetic cell death due to the etching of the oxide shell in acidic environment.[78] Therefore, highlighting the potential of these core material in theranostics applications.

4.1.8. Iron carbide (Fe_5C_2). MNPs made of other iron compounds have already attracted significant attention in biomedical applications due to unique magnetic properties. For instance, the potential of multifunctional iron carbide (Fe_5C_2) NPs for MRI-guided photothermal therapy with the purpose of diagnosis and treatment of cancer was previously highlighted by Hou and co-workers.[86] Indeed, they discovered that Fe_5C_2 NPs with overall diameter of 20 nm displayed a superparamagnetic regime with high saturation magnetisation around 125 emu g^{-1} at ambient temperature.[86] Fe_5C_2 NPs could induce stronger *hypo*-intensities compared to Resovist due to higher magnetisation.[86] The transverse relaxivity (r_2) was also calculated to be 312 mM^{-1} s^{-1} and 174 mM^{-1} s^{-1} for Fe_5C_2 and Resovist respectively. The higher potential of Fe_5C_2 NPs make these NPs more efficient as contrast agents in MRI.[86] Due to unique properties such as superparamagnetism, high saturation magnetisation, monodispersity, small particle sizes, good stability, and efficient photothermal effects; Fe_5C_2 NPs can also work as an ideal platform for designing MPI tracers with cancer theranostic applications.

4.1.9. Iron–Cobalt alloy (FeCo). Owing to their high saturation magnetisation and multifunctional features, FeCo NPs also attracts considerable attention as potential core material for MPI in theranostic applications. In a study conducted by Dai and co-workers, it was shown that FeCo/graphitic-shell nanocrystals with the size of 7 nm have the highest saturation magnetisation (215 emu g^{-1}) among magnetic nanocrystals.[87] In a recent study, Song *et al.* demonstrated that carbon coated FeCo NPs with a core diameter of 10 nm can achieve an M_{sat} value of around 192 emu g^{-1}. These NPs also displayed great performance in MPI when compared to Vivotrax and Faraheme with sixfold and fifteenfold enhancement in signal intensity respectively. Therefore, FeCo NPs hold great promises as ideal MPI tracers for MPI-guided cancer therapy due to their photothermal and magnetothermal properties.[13]

4.1.10. Selection of magnetic material. In summary, magnetic MNPs such magnetite, metal ferrites, zero valent iron NPs and maghemite all present unique and interesting properties which would make them ideal for MPI tracers. However, in addition to satisfying all the key requirements for MPI, researchers also must consider the intended applications in order to choose an appropriate MNP material. For example, cobalt ferrite is best to be used for MPI coupled with hyperthermia therapy due to their high heating performance compared to other MNP materials. In applications involving drug delivery and cancer cell targeting, manganese ferrite NPs are the most suitable as they are biocompatible, highly magnetic and can also exhibit toxicity towards HeLa cancer cells. Finally, for applications that require very small particles (<20 nm), for example in crossing the blood–brain barrier, zero valent iron cores are promising MNP tracers with high MPI performance. Therefore, applications play an important role in the decision process of choosing and designing an ideal tracer that can satisfy all the requirements.

4.2. Synthesis of MNPs

Solution phase synthesis using thermal decomposition is the preferred method for producing MNPs due to the ease in adjusting the synthetic conditions to produce controlled size and shapes. The synthesis generally involves the thermal decomposition of an iron precursor in a solution containing surfactants, reducing agents and solvents at an elevated temperature. This method is easy to control, cost effective and can produce highly crystalline nanoparticles with narrow size distributions.

Fig. 5a shows the synthetic approaches for different types of magnetic iron/iron oxide MNPs *via* thermal decomposition. In thermal decomposition synthesis, an iron precursor is heated in a solution containing a reducing agent, to assist the formation of lower oxidation state iron, and surfactants, that bind to iron monomers during growth and stabilise the resulting MNPs. By controlling these variables, the nucleation and growth processes can be tuned to produce single crystalline, size-controlled MNPs. Slight variations or additions to this general synthetic approach enable different types of MNPs to be accessed, as outlined in the following sections.

4.2.1. Magnetite. The phase-controlled synthesis of magnetite is typically achieved from the controlled oxidation of wüstite NPs.[59,88] By controlling the oxidising conditions, magnetite can be prevented from further transformation into a higher oxidation state phase like maghemite or hematite. The oxidation approach and precursor selection are of paramount importance to synthesis of size controlled and phase-pure magnetite NPs. In this approach, wüstite NPs are synthesised by reducing organic precursors containing cationic iron centres such as iron(III) acetylacetonate [$Fe(acac)_3$] or iron oleate.[24,89–91] A controlled addition of mild oxidiser, such as air, under elevated temperatures, is then required to slowly oxidise the MNPs to magnetite with control of the stoichiometry of final product. With long oxidations times, up to 90 minutes, the phase selectivity will favour magnetite with composition of more than 98% magnetite for monodisperse NPs at 15 nm.[92]

In general, organic solvents produce MNPs with better size and shape control compared to MNPs synthesised in aqueous solutions.[90] It is also possible to use an indirect method of

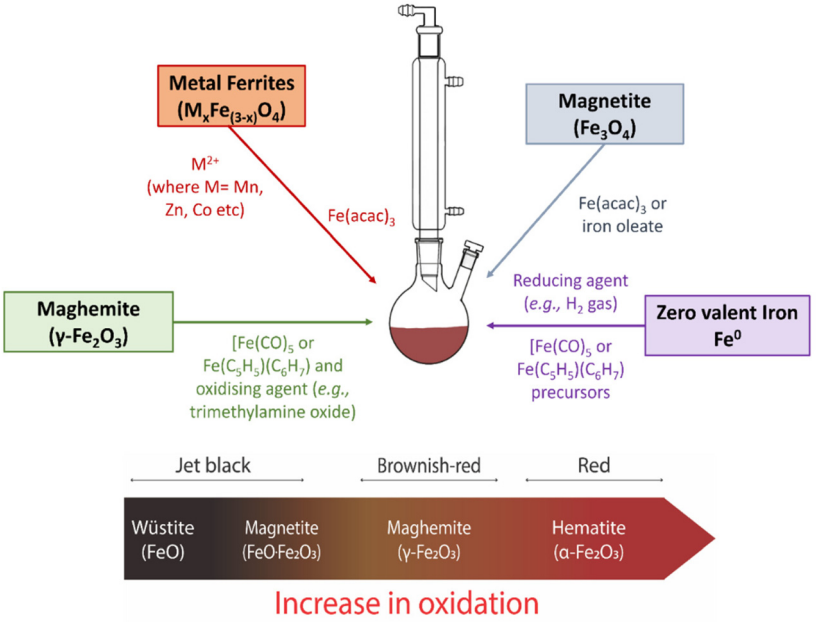

Fig. 5 Illustration of a typical setup for the synthesis of MNPs *via* thermal decomposition with surrounding boxes indicating the specific precursors and other variables that must be controlled to form each material type. The arrow at the bottom illustrates the different colours of the MNP types that are observed when oxidising the MNPs after the thermal decomposition synthesis.

synthesis by reducing iron oxides or oxohydroxides such as hematite and geothite to magnetite.[88] However, the gradual oxidation of magnetite to maghemite causes NPs to typically consist of a mixture of both phases.[93,94] Due to the high similarity of lattice spacing and crystal structure of magnetite and maghemite, it is hard to distinguish between these two phases. Complementary characterisation techniques such as X-ray diffraction, Raman and Mössbauer spectroscopy are generally required.[59,94–97]

4.2.2. Metal ferrites and zero-valent iron. High quality metal ferrite nanoparticles can be produced by employing similar experimental parameters as magnetite but extending the oxidation process. As depicted in Fig. 5, the key difference between these two procedures is the introduction of a metal dopant. The dopant M^{2+} is usually an organometallic precursor $M(acac)_2$, where M represents any metal (usually transition metal) of interests such as Mn, Zn or Co. The metals are chosen based on the desired properties and the intended applications.

Similarly, iron zero valent NPs surrounded by an iron oxide shell can also be synthesised by using slow thermal decomposition of iron pentacarbonyl $[Fe(CO)_5]$ or $Fe(C_5H_5)(C_6H_7)$ precursors.[26,80,84] However, as iron is a highly reactive species, the synthesis of $Fe@Fe_3O_4$ is carried out under inert atmosphere using hydrogen gas as the reducing agent. By preventing oxidation by air, the zero-valent iron phase is achieved.

4.2.3. Maghemite. Maghemite can either be formed directly in solution or by the oxidation of pre-formed magnetite NPs. Hyeon and co-workers developed a method to directly form monodisperse and uniform maghemite NPs without a further size-selection process with a size of 13 nm by direct injection of $Fe(CO)_5$ into a solution containing surfactant and trimethylamine oxide.[98] Hyeon and co-workers also used this trimethylamine oxide agent to oxidise monodisperse iron NPs at 300 °C to produce 2D hexagonally close-packed 11 nm maghemite.[95] This indirect method is typically preferred because it allows easy control over particle size as well as better reproducibility with a yield of over 80%.[98]

Trimethylamine oxide $[(CH_3)_3NO]$ acts as an oxygen transferring agent that offers a better and more versatile means for controlling the oxidation process as compared to air.[95,98] Moreover, the thickness of iron oxide layers and crystallinity of NPs can be easily tuned by $(CH_3)_3NO$. In contrast, using air as an oxidant results in uncontrolled oxidation, which decrease control over thickness of iron oxide layers, poor uniformity of crystalline phases, rapid agglomeration, lack of crystallinity, and formation of magnetically dead layers.[99–102] Following the oxidation with post-synthesis annealing is an indispensable part of the synthesis protocol to enhance the crystallinity of maghemite NPs.[59]

Size plays an important role on the dominant phase of the SPIONs. When oxidising MNPs, the iron oxide phase ratio of magnetite to maghemite is dependent on the particle size and oxidative conditions of the iron oxide phase. MNPs tend to favour the magnetite phase at larger diameters while favouring the maghemite phase at smaller diameters during the process of oxidation. At the nanoparticle level, the mechanism of oxidation at room temperature follows a progression from zero valent iron to FeO which transforms into Fe_3O_4 and then Fe_2O_3 (Fig. 5). With larger diameters, the oxidation process transforming magnetite to maghemite is slower due to having a smaller surface to volume ratio.[103–105]

Only a few other methods have been reported to successfully form maghemite NPs. For example, Teng *et al.* synthesised highly monodisperse maghemite NPs with very small (~3 nm) diameter. Maghemite NPs were synthesised through thermal decomposition of iron carbonyl in octyl ether in the presence of stearic acid as surfactant at a certain molar ratio.[106] Moreover, maghemite NPs can be produced *via* oxidation of magnetite at 240 °C in air followed by a decrease in temperature to 50 °C when the size reaches to the nanoscale.[88] Dehydration of lepidocrocite (γ-FeOOH) can also be conducted to obtain maghemite NPs.[88]

4.3. Synthetic parameters

For all MNP materials, size control is essential for producing uniform signals and high resolution MPI images. Several approaches have been directed towards precisely controlling the NPs size. In particular, the extended LaMer's mechanism and reversible magnetic agglomeration proposed by Huber and co-workers, offers several advantages such as good reproducibility, predictability, and scalability.[42] The extended LaMer mechanism works by continuous addition of precursor to the reaction solution after nucleation. This keeps the concentration of iron atoms high so that the growth rate remains constant, Ostwald ripening is avoided, and the size of NPs can be predictably controlled by changing the reaction time.

4.3.1. Type of precursor. Several studies highlighted the importance of specific reaction conditions in the synthesis protocol to achieve highly uniform, single crystalline, stable MNPs. The most effective parameters for achieving synthetic control include the type and concentration of precursor, type of surfactant, molar ratio of surfactant to precursor, heating rate, reaction temperature, and stirring speed.[59,88,104,106,107] For instance, Hufschmid *et al.*, reported that while $Fe(CO)_5$ precursor is especially suitable for synthesis of SPIONs smaller than 10 nm through thermal decomposition, iron(III) oleate $[Fe(C_{18}H_{33}O_2)_3]$ and iron oxyhydroxide (FeOOH) are best suited to the synthesis of larger ones with sizes ranging from 10 to 30 nm.[59] Sun *et al.*, showed that the high temperature (265 °C) reaction of $Fe(acac)_3$ in phenyl ether in the presence of oleic acid, OLA, and alcohol can result in monodisperse magnetite NPs.[108] In order to produce larger magnetite NPs, a seed-mediated approach is preferred to encourage growth of smaller magnetite NPs into larger ones with diameters of up to 20 nm.[108]

4.3.2. Temperature. In general, high reaction temperatures <200 °C are used to produce SPIONs in order to thermally decompose the iron precursor. High reaction temperatures also ensure fast nucleation bursts to achieve monodisperse samples. Recently, Cheah *et al.*, investigated the role of reaction temperature in controlling the size of SPIONs synthesised by thermal decomposition of $Fe(acac)_3$ in diethylene glycol (DEG) as a polyol solvent. It was shown that at reaction temperatures lower than 235 °C, NPs tend to be highly water dispersible and larger NPs can be produced by increasing the reaction temperature. However, at temperatures around boiling point of DEG (245 °C), aggregation and precipitation dominate.[107]

4.3.3. Reaction time. In the thermal decomposition method, the reaction time is crucial in controlling the particle size, morphology, and magnetic properties of SPIONs.[109] In a study conducted by Yang *et al.*, it is shown that just by adjusting the reaction period from 0.5 h to 5 h can effectively increase the size of magnetite NPs from 52 nm to 79 nm under the same conditions.[109] In addition, the study also showed the importance of reaction time in changing the morphology of the nanoparticles and generate NPs with a more uniform shape.[109] As a result of larger particle size as well as shape anisotropy, the saturation magnetisation of NPs increased linearly from 77.4 to 101.1 emu g^{-1}. It should be noted that due to interdependent effects, the role of the solvent should be taken into consideration when evaluating the impact of reaction time.[109] For example, Lu and co-workers studied the effect of reaction time and type of solvents on particle size and morphology of cobalt ferrite ($CoFe_2O_4$) NPs.[110] They demonstrated that the size and shape of cobalt ferrite NPs synthesised in di-octyl ether with equimolar amount of oleic acid and oleylamine at 620 mM change significantly by increasing the reaction time from 1 min to 120 min at 287 °C.[110] Furthermore, by increasing the reaction time from 1 min to 10 min and then 120 min, 4.3 nm spherical NPs transformed into 16.1 nm cubic NPs and then 28.1 nm star-like NPs. However, by changing the solvent from di-octyl ether to 1-octadecene, the particle shape remained the same (spherical) and only particle size increased from extending the reaction time.[110]

4.3.4. Surfactant. There are a variety of surfactants that can be used as tools to control the size and crystallinity of SPIONs. In organic solutions, surfactants with long alkyl chain tails and hydrophilic head groups are used. Oleylamine is chemisorbed as an amine onto the iron oxide surface and decomposes at a high temperature of 250 °C. Oleic acid is a carboxylate that is chemisorbed to the surface of SPIONs using a monodentate ligand.[111] Oleic acid decomposes slowly over a wider range of temperatures. The head of oleic acid, the carboxylate linker, is still retained even when oleic acids long aliphatic tail decomposes. Hence, oleic acid is best used in a co-surfactant system with oleylamine or another amine surfactant to effectively protect NPs from oxidation when exposed to air.[112] In a study, the average size of magnetite NPs increased by reducing the concentration of oleic acid in the reaction mixture.[113,114] Very small (~3 nm) maghemite NPs were also synthesised by replacing the oleic acid with stearic acid through thermal decomposition of $Fe(CO)_5$.[106]

In aqueous syntheses, polyvinyl alcohol (PVA) and polyvinylpyrrolidone (PVP) are excellent surfactants for stabilising MNPs against aggregation and preventing over-oxidation compared to smaller surfactants such as anionic sodium cholate.[115] PVA is an uncharged high-performing polymer that is biocompatible and biodegradable. Coating with PVA has shown to decrease the M_{sat} in comparison to uncoated SPIONs and so may not be viable for MPI compared to other alternatives.[116] PVP is another large surfactant that gives SPIONs high stability in aqueous solutions. It also improves the crystallinity of the SPIONs by preventing defect formation when employed

during co-precipitation synthesis. PVP, commonly creates a magnetically dead layer and gives a lower M_{sat} of 50 emu g^{-1}.[100,117]

Cationic cetyltrimethylammonium bromide (CTAB) surfactant is effective during aqueous MNP synthesis as it bonds with the anionic surface of SPIONs, effectively capping the particle from other interactions. However, CTAB coated SPIONs are more vulnerable to oxidation, typically transforming magnetite to maghemite and allowing agglomeration to produce larger SPIONs over time.

4.4. MNP morphology

The quality of MPI signal does not only depend on the size of NPs, but also on their morphology. The morphology dictates how the magnetic spins align within the MNP and at the surface. For example, cube-shaped SPIONs possess higher spin ordering at the surface than spherical MNPs, leading to a higher overall magnetic moment and M_{sat} values. The quality of MPI signal does not only depend on the size of NPs, but also on their morphology. The morphology dictates how the magnetic spins align within the MNP and at the surface. For example, cube-shaped SPIONs possess higher spin ordering at the surface than spherical MNPs, leading to a higher overall magnetic moment and M_{sat} values.[19,26,118]

Langevin theory only describes the dependence of MPI signal on the MNP size of mono-domain NPs without considering the consequences of shape anisotropy.[119] Among types of anisotropy (crystal, shape, and strain), shape anisotropy is the key factor for designing high performance MPI tracers. Shape anisotropy has a dominant influence on the coercivity of magnetite and maghemite NPs, leading to a drastic change in the magnetisation curve.[120] However, shape anisotropy can impact the MPI performance beyond this. Weizenecker *et al.* simulated the correlation between anisotropy and MPI signal considering the various anisotropic NPs with different MNP sizes. It was shown that increasing the anisotropy of NPs drastically weakens the MPI signal so that only NPs with small shape anisotropy can optimise the MPI performance.[119] Bauer *et al.* investigated the effect of shape of SPIONs on the MPI signal. They demonstrated that spherical magnetite NPs (19 nm) show higher performance in MPI compared to cubic ones (15 nm) due to SNR enhancement. This is most likely due to the higher tendency of cubic SPIONs to form chain-like arrangements.[19] In addition, the higher shape anisotropy of cubic magnetite NPs resulted in asymmetry of PSF diagram (3.6 mT peak shift), revealing detrimental effect of cubic shape SPIONs on the MPI signal.[19] Moreover, magnetite multi-granule nanoclusters with optimal particle size and granule diameter have also been demonstrated as potential MPI-tailored tracers.[121] Overall, the effect of MNP morphology on MPI signal does not precisely mirror changes in the hysteresis curves and would benefit from further research in this area.

Many design strategies have already been proposed to produce SPIONs with various shapes including spherical, cubic, octopod, elongated, disk-shaped, and flower-like with different levels of anisotropy.[88,122] Spherical (NS) and octopod (NO) morphologies of iron oxide NPs with different sizes and different shape anisotropies can synthesised by thermal decomposition of iron stearate in the presence of oleic acid in dibenzylether.[123]

Surfactants, precursor concentration and temperature are the most effective synthetic tool for the shape-controlled synthesis of SPIONs due to their key role in directing the nucleation and growth stages.[88] For instance, Kovalenko *et al.* synthesised SPIONs with spherical and cubic shapes by controlling the ratio of oleic acid and sodium oleate in the reaction mixture as well as reaction temperature.[124] In a study by Cotin *et al.*, the effects of precursor as well as the amount of sodium oleate surfactant, and heating rate on the shape of NPs were investigated.[122] Low monomer concentration and high temperatures were found to lead to more isotropic nanostructures.[88] Although the morphology can be finely controlled in synthesis,[24,26,85,125] further studies into the effect on MPI signal are needed.

5. Surface modification of MNP for MPI

Surface modification is one of the most important factors in MPI tracer design as it is responsible for the fate of MNPs *in vivo*. MNPs are usually synthesised in organic solvents in order to precisely control the shape, size and composition of NPs. However, the MNPs synthesised in organic solvents are generally coated with hydrophobic oleic acid or oleylamine surfactants.[82] Hence, they are not suitable for biological applications as they have poor biodistribution and water dispersity. Therefore, surface modification is important to improve the aqueous dispersibility and the blood circulation time of MNPs *in vivo*. For biological and biomedical applications in MPI, it is vital for the MNPs to be non-toxic, highly biocompatible, stable in aqueous media and have long circulation time in the body.

MNPs are generally administered *via* intravenously injection to accumulate at the target site. The retention time of the MNPs will vary depending on their surface chemistry and the size of NPs. Coatings such as biomolecules and biocompatible polymers can prolong the circulation time of these MNPs *in vivo* as they are inert to the blood proteins and hence can delay the clearance of these MNPs.[126,127] Depending on the applications, these MNPs will be modified with a suitable surface chemistry to either accumulate at the target organ or circulate in bloodstream around the body. If they circulate in the bloodstream, it is possible for them to bind to proteins making them recognisable by macrophages and so be eliminated from the body.[126]

The type of surface ligands used will dictate the hydrodynamic size of the MNPs. The pharmacokinetics, cellular uptake and biodistribution of the MNPs are dependent on this resulting hydrodynamic size.[57,128] Studies have found that the optimal hydrodynamic size range for an improved lifetime of SPIONs in the bloodstream is between 15 nm and 100 nm.[6]

This size range was determined based on the size of the kidney fenestrae (~15 nm) and the size of the sinusoidal capillaries in the liver and spleen (~50 nm – 180 nm).[6] Therefore, within this range, NPs will be more likely to escape excretion by the kidney and immediate clearance from the reticuloendothelial system (RES).

Apart from making the nanoparticles dispersible in aqueous solutions, there are three main goals when it comes to coating MNPs, which are (I) stabilisation of MNPs against aggregation, (II) prevention of oxidation and (III) addition of further functional groups for water dispersibility or additional functionalisation (Fig. 6). In this section, different type of coatings will be discussed, and we will also be presenting our insights on the appropriate uses of these coatings.

5.1. Stabilisation of MNPs against aggregation

Aggregation is one of the most common problems for MNPs as they have low colloidal stability that can adversely affect the MPI performance as well as causing blood clots. In order to eliminate this problem, certain coating options can be used to improve the dispersity of MNPs in solution and prevent aggregation. There are a wide range of options for this type of stabilisation that include small molecules to bulky polymers.

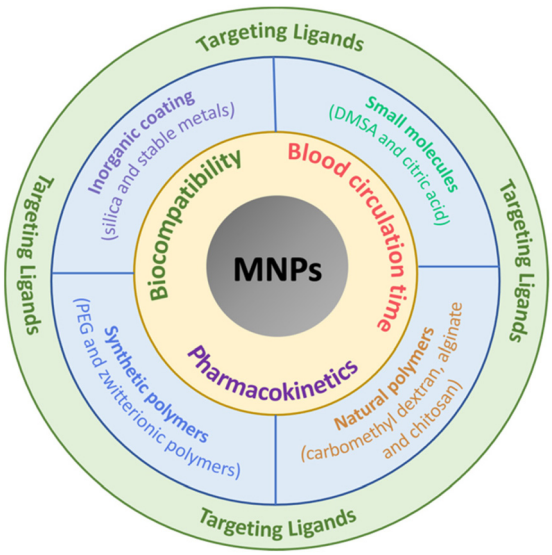

Fig. 6 Illustration of a coated MNP with different surface modification strategies for MPI tracers.

5.1.1. Dimercaptosuccinic acid (DMSA). DMSA is the most commonly used small molecule to stabilise and improve the biocompatibility of MNPs in physiological environments. Owing to the strongly binding oxygen groups onDMSA, it can easily displace weakly binding surfactants coated on MNPs *via* a simple ligand exchange reaction. DMSA coated NPs have excellent biocompatibility, show no signs of cytotoxicity and can achieve high stability in biological media for up to 6 months.[26,84,129] In a recent study conducted ▣Citoglu *et al.*, it was reported that 25 nm cubic SPIONs coated with DMSA possess a higher magnetisation compared to unmodified SPIONs (coated with decanoic acid).[130] The increase in M_{sat} (DMSA coated = 89.6 emu g^{-1} and unmodified = 74.2 emu g^{-1}) is hypothesised to be due the disulfide bonds from the DMSA molecule that can shorten the distance between MNPs and hence improve the magnetic properties (Fig. 7).[130] Furthermore, the free thiol and carboxylic groups of DMSA can be conjugated with antibodies, proteins or other drugs for biomedical applications.[129] However, Liu *et al.* reported that DMSA coated MNPs could degrade into iron ions in an acidic environment inside the lysosome.[131] This degradation will result in high concentration of iron accumulated in the body that can produce reactive oxygen species and thus lead to cell toxicity.[130] As a result, these DMSA coated NPs can be used in therapeutic treatment to target cancerous cells in mildly acidic environments only (*i.e.*, 6.4 pH – 7.0 pH). Therefore, DMSA coated magnetic nanoparticles present great potential for uses in therapeutic treatments such as cancers and anaemia.

5.1.2. Tricarboxylic acid or citric acid. Tricarboxylic acid or citric acid (CA) are other good small sized surfactant to coat MNPs for biological applications. In the study conducted by Li *et al.*, it is stated that CA coated Fe_3O_4 NPs showed negligible changes in the hydrodynamic size compared to uncoated SPIONs.[132] For this reason, the M_{sat} of the two sizes CA coated SPIONs (9 nm NPs = 50 emu g^{-1} and 25 nm NPs = 46 emu g^{-1}) were determined to be almost the same as the M_{sat} for the

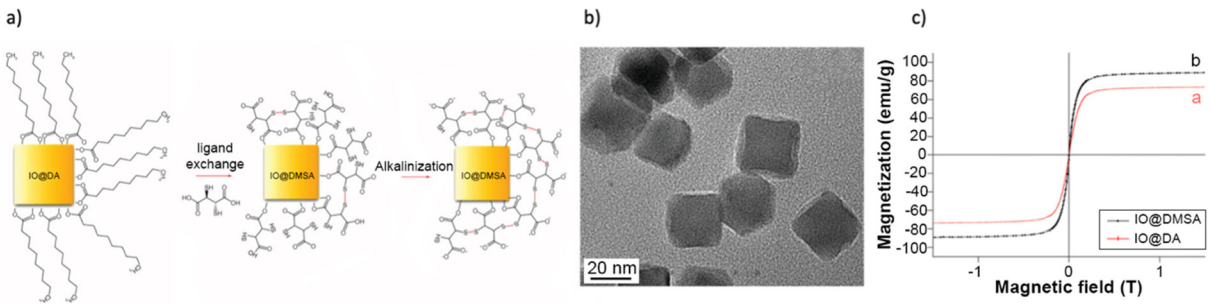

Fig. 7 (a) Schematic illustration of the surface modification of cubic iron oxide nanoparticles with DMSA *via* ligand exchange, (b) TEM images of DMSA coated cubic NPs and (c) magnetisation curve showing the saturation magnetisation of uncoated (IO@DA – shown in red) and DMSA coated (IO@DMSA – shown in black) NPs.[130] This figure has been reproduced from ref. 130 with permission from Nanomedicine, copyright 2022.

uncoated counterparts (9 nm NPs = 51 emu g^{-1} and 25 nm NPs = 46 emu g^{-1}). The study also reported that the 25 nm CA coated MNPs exhibit a lower coercivity value of 38 Oe compared to uncoated 25 nm NPs of 46 Oe. This shows that the CA coatings not only preserve the magnetic properties of the SPIONs but also reduce the coercivity of the NPs with sizes that are close to 25 nm, which is highly beneficial for producing high quality MPI signals. In addition, citric acid coatings can also prevent the MNPs from clustering and oxidation, which are important properties for *in vivo* application.[75]

5.1.3. Biopolymer coatings. Biopolymer coatings such as carboxymethyl dextran and alginate are also highly desirable to increase the water dispersity of MNPs due to their biodegradability and biocompatibility. Carboxymethyl dextran (CMD), a naturally made polysaccharide, has been widely used to stabilise many MNPs in laboratory as well as commercial tracers including Resovist®.[133] Studies have also shown that MNPs coated in CMD displayed an improved cellular uptake due to its negative surface charge and negative zeta potential (approximately − 32.8 mV).[134] The high cellular uptake enabled these coated MNPs to be employed in applications such as drug delivery and single cellular tracking using MPI or MRI.[135] Furthermore, owing to their non-immunogenic biopolymeric nature, CMD has also been used as an antithrombotic agent in medicine to reduce blood viscosity.[136] However, these MNPs showed uptake in the liver and spleen hence making them unsuitable for *in vivo* imaging applications.

Similarly, alginate, another polysaccharide derived biopolymer, can also provide MNPs with a negative surface charge coating which can prevent these coated NPs against aggregation due to electrostatic repulsion. Therefore, these alginate coated MNPs are also mainly used for drug delivery applications.

5.1.4. Chitosan. Apart from the above biomacromolecules, chitosan has also been explored for the coating of MNPs for many biomedical applications, especially drug delivery. As a natural polyaminosaccharide, chitosan consists of many hydroxyl and amine functional groups which allows these coated NPs to be easily conjugated with various drugs and antibodies.[137] Kim *et al.* showed that the 15 nm chitosan coated MNPs displayed a high M_{sat} value (83 emu g^{-1}) and an improved signal intensity in MPI.[138] Furthermore, due to the presence of the amino groups that are prone to protonation, chitosan is shown to be quite soluble in acidic environment such as biological media hence making these coated MNPs suitable for drug delivery applications.[137] Arias *et al.* successfully demonstrated the capability of these chitosan encapsulated MNPs as a carrier of gemcitabine drug to tumour cells. The study showed that these Fe_3O_4/chitosan composites displayed a greater drug loading capacity and could be triggered to release the chemotherapy drugs in low pH environment of tumours.[139] This study further emphasises the potential of chitosan coated MNPs to be employed in drug delivery applications.

5.1.5. Polyethylene glycol (PEG). PEG is the most commonly used polymer to coat MNPs for biological uses. They are well-known for their biocompatibility, non-toxicity, water-solubility and prolonged circulation time.[10,25,57,128,140] PEG also has high water-binding capacity that makes it resistant to non-specific adsorption of proteins and cells hence improving its selectivity while remaining unrecognised by the immune system.[141] This makes PEGylated MNPs good candidates for drug delivery applications. However, it has been suggested that the continuous injection of PEG may lead to the induction of anti-PEG immunoglobin M (IgM) antibodies.[142] Despite this, PEG has been highly successful for a range of NPs and is the most widely used coating for *in vivo* analysis.

In order to improve PEG coated NPs performance *in vivo*, some studies have investigated the effect of grafting density and molecular weight of PEG on their pharmacokinetics. Krishnan and co-workers reported that SPIONs coated with 20k Da PEG at a loading density of 18.8% (LS-008) had a much longer blood half-life of 105 min compared to one with a loading density of 12.5% (*i.e.*, 26 min).[140] When the molecular weight of PEG was reduced to 5k Da at the same loading density (18.8%), the NPs possessed an even longer blood half-life of 155 min[140] However, due to insufficient coating from using a lower loading capacity, the majority of the MNPs aggregated during the coating process which resulted in a much lower yield.[140] Furthermore, in a different study conducted by the same group, Krishnan and co-workers reported that the terminal group on PEG can influence the biodistribution and blood circulation time of NPs *in vivo*.[2] In that study, they compared the bi-functional PEG (NH_2-PEG-NH_2) with NH_2-PEG-FMOC in terms of blood half-life, hydrodynamic size and MPI performance. NH_2-PEG-FMOC was shown to have a smaller hydrodynamic size (43 nm), better MPI performance and a longer circulation time (about 23 min − 26 min) compared to the bi-functional PEG (size = 98 nm and $T_{1/2}$ = 12 min) (Fig. 8).[2] In another recent study, Rinaldi-Ramos and co-workers showed that NPs coated with a brush of PEGsilane achieved an excellent MPI performance and long blood half-life of approximately 7 hours which is much longer than any available commercial tracers (Fig. 9).[143] This makes PEGsilane coated NPs an excellent candidate for MPI applications that require long circulation time such as cell labelling, blood pool imaging and leukemia studies.

5.1.6. Zwitterionic polymers. In recent years, many researchers around the world have been investigating the potential of zwitterionic polymers as a surface coating for MNPs in biomedical applications. Zwitterionic polymers have both positively and negatively charged groups incorporated into the polymer backbone. For this reason, zwitterionic polymers display high colloidal stability and water dispersity over a wide range of pH values and ionic strengths. In addition, they reduce nonspecific binding to proteins hence improving the circulation time of NPs *in vivo*. Pombo-Gracia and co-workers reported that the SPIONs encapsulated with zwitterionic polymer poly (maleic anhydride-*alt*-1-decene) functionalised with 3-(dimethylamino) propylamine (PMAL) exhibit minimal cytotoxicity, possess high colloidal stability in a wide range of pH and ionic strengths media. In addition, no indication

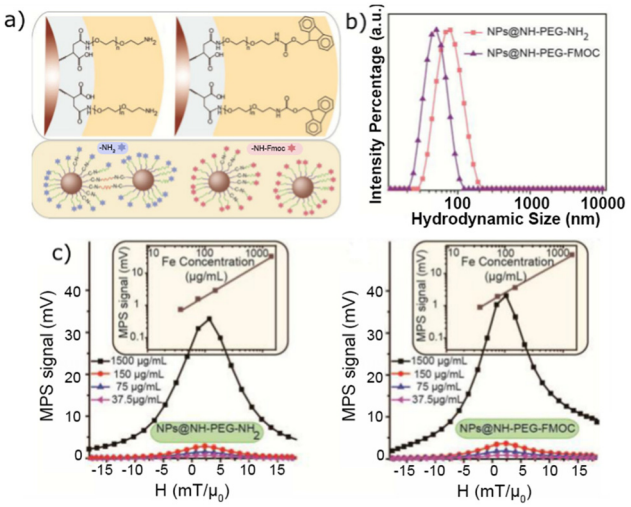

Fig. 8 (a) Magnetic measurements of iron oxide nanoparticles functionalised with NH_2-PEG-NH_2 and NH_2-PEG-FMOC directly taken at different time of post-injection (from 0 min to 60 min). (b) MPS signal showing the MPI performance of the bifunctional and hetero-functional PEG magnetic NPs at different time after injection. (c) Blood half-lives of the NPs with two types of PEG surface determined by the VSM (shown in red) and MPS (shown in black).[2] This figure has been reproduced from ref. 2 with permission from Biomaterials, copyright 2022.

inflammatory response or haemolytic activity *in vitro* and negligible cellular uptake by phagocytic and non-phagocytic hepatocarcinoma cells was observed.[144] Therefore, the PMAL coated SPIONs can achieve high selectivity after functionalisation with specific proteins and are an ideal candidate for cell targeting applications.

5.2. Stabilisation of MNPs against oxidation

Apart from aggregation, oxidation is another common problem among MNPs *in vivo* because it can adversely affect the M_{sat}, especially for MNPs with lower oxidation state iron such as zero-valent iron or magnetite. This reduction in magnetic properties consequently lowers the signals generated and image resolution in MPI. Therefore, it is important to provide an appropriate surface coating to prevent the MNPs from oxidising. The best strategy would be to encapsulate these MNPs so that they cannot interact with any oxygen species in solution or biological media. As many of the coatings described in the previous section are permeable by oxygen, the most common option for this type of stabilisation is inorganic coating with silica or stable metals.

5.2.1. Inorganic coating, silica. Silica (or SiO_2) is one of the most widely used material to provide protection as well as improving the biocompatibility, stability, and water dispersity of MNPs for biomedical applications. The silanol terminal group on silica coated MNPs allow surface functionalisation with various peptides, proteins, and antibodies. Chen *et al.* discovered that when PtFe metal alloy was coated with silica, they can be internalised by tumour cells and show no signs of cytotoxicity for 7 days of incubation at 30 μg mL^{-1}. Furthermore, it was also found that these PtFe-silica NPs also are strong T_2 contrast agents hence confirming the potential of these NPs to be used for cellular and *in vivo* imaging, hyperthermia, stem cell therapy, drug delivery and regenerative medicine.[145] In a recent study, Nasiri *et al.* functionalised SPIONs@SiO_2 with papain (PPN) as an anticancer agent, and the results show that SPIONs@SiO_2-PPN can successfully reduce cell viability and have a higher percentage of apoptosis for HeLa cells when compared to the native PPN (Fig. 10).[146] This study shows that the coating of silica onto NPs holds great potential as a drug delivery vehicle in cancer therapy.

However, the presence of the diamagnetic silica layer can reduce the magnetisation of the overall MNPs. Studies have shown that at low temperatures, the M_{sat} of the silica coated MNPs can be decreased by 32% (from 31 emu g^{-1} to 21 emu g^{-1}) under the magnetic field of 1 kOe (or 0.1 T).[147] It was also shown that the silica coating also affects the Curie temperature (T_c) and cause a T_c decrease of 7% (341 K to 317 K).[147] Although, not significant for MPI, this significant drop of temperature can limit the MNPs use as dual imaging-treatment tracers in hyperthermia treatment. If both MPI and treatment are desired, it is important to carefully control the thickness of silica coating to only be thick enough to ensure biocompatibility and water stability while keeping the M_{sat} as high as possible to conserve the heating efficiency.

5.2.2. Gold coating. Besides silica, metals can also be used to protect magnetic nanoparticles against oxidation and enhance their performance in biomedical applications. This is especially useful for air sensitive materials (*i.e.*, Fe^0 NPs) since other coating options require the NPs to be dispersed in aqueous solvents, which can cause a small degree of oxidation before coating. Therefore, if the SPIONs can be coated with a metal layer in an inert environment, this can protect the MNPs from oxidation and maintain their superb magnetic properties. Furthermore, metals are also excellent conducting materials and can induce heat under an AC magnetic field. This makes metallic coatings more frequently used for hyperthermia treatment.

Owing to its non-toxicity, non-immunogenicity and ease of conjugation with many biomolecules, gold has attracted attention as the optimal metallic coatings for MNPs. Gold delivery applications.[148–150] Wagstaff *et al.* further confirms the potential of these Au@FeNPs as drug delivery vehicles; they were coating can improve the biocompatibility of MNPs and reduce aggregation by steric and electronic repulsions. Studies have shown that the gold coatings also have no significant effect on the magnetic properties of NPs and can sustain drug release; making these gold coated SPIONs ideal candidates for drug successfully delivered drugs to the tumours and was shown to be 4.3-fold more effective than cisplatin (*i.e.*, achemotherapy drug that is used to treat cancer) alone.[149] However, directly coating the surface of MNPs with gold can be synthetically challenging due to the differences in their crystal structures and lattice measurements.[151] A Au shell can be indirectly coated onto MNPs by introducing a "glue material" between the core and the Au shell to ease the lattice differences

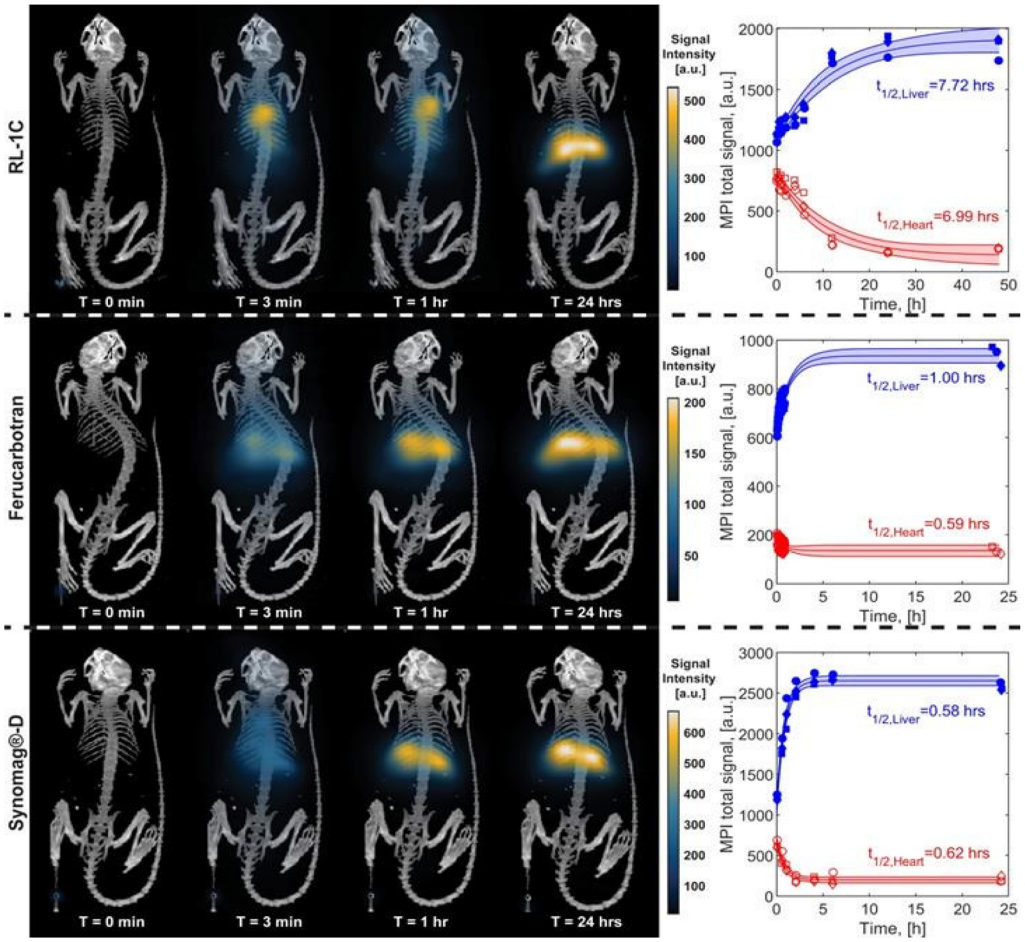

Fig. 9 MPI/CT scans for three different samples RL-1C (a PEGsilane coated MNP), Ferucarbotran and Synomag®-D to show the MPI performance of these NPs at different time after injection (from 0 min to 24 h) and the blood half-life of these nanoparticles in the heart and liver.[143] This figure has been reproduced from ref. 143 with permission from Nanotheranostics, copyright 2022.

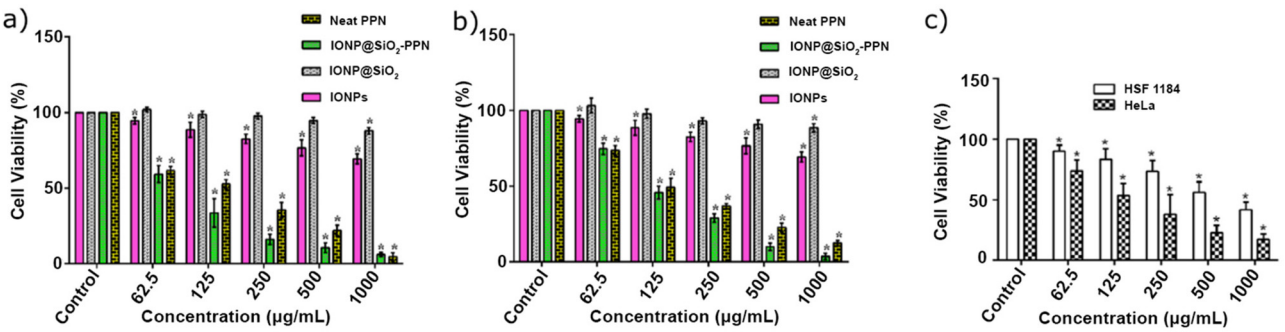

Fig. 10 MTT assays showing the cell viability charts for neat papain (PPN), IONPs@SiO_2-PPN, IONPs@SiO_2 and pure IONPs by using (a) HeLa cell lines, (b) HSF 1184 cell lines and (c) cisplatin. The asterisk symbol (*) indicates significant differences between these results compared to the control analysed by unpaired *t*-test and followed by Holm-Sidak *post hoc* test ($p < 0.05$).[146] This figure has been reproduced from ref. 146 with permission from Nanotechnology, copyright 2022.

between the two materials.[152] Since the coating of Au shell onto silica is well established, SiO_2 is mostly used as an intermediate layer between Au shell and MNPs.[24] Although the extra silica layer can reduce the M_{sat} of the material, the Au@silica@SPIONs were shown to be possess a highly tuneable plasmon resonance in the near infrared region (a.k.a. NIR) and hence can mediate photothermal ablation to tumours and cancer cells.[153,154]

5.3. Coating for additional functionality

For a more specific application such targeted imaging and drug delivery, it is vital for MNPs to be further functionalised with either antibodies, proteins, or drugs to successfully bind to the desired targets. For example, a study that is focused on cancer treatment might require MNPs to be conjugated with cisplatin or other drugs. Whereas another study may require MNP conjugation with specific antibodies so that it can attach to a targeted protein.

In a dementia study, it is found that the main cause of Alzheimer's disease is caused by the production and build-up of beta amyloid (Aβ) proteins around brain cells.[155] This hinders signal transmissions which lead to a decrease in neurotransmitters. Over time, these areas shrink and results in symptoms such as memory loss, difficulties in judgement and even the ability to perform simple tasks. Therefore, to successfully image the brain for build-up of Aβ proteins, MNP tracers are required to be functionalised with anti-Aβ antibodies so that they can attach to the amyloid plaques. The majority of the antibodies, proteins and drugs can be easily conjugated onto MNPs coated with either inorganic or organic for MPI tracers to be further modified with the suitable antibodies or drugs to fit the intended application.

6. Applications of MPI

Owing to its unique properties, MPI has many advantages that make it highly desirable for many biomedical applications such as *in vivo* imaging, cellular tracking, and thermal guided cancer therapy. MPI can also be used for targeted imaging and therapeutic treatments if using proper conjugation chemistry with suitable proteins, antibodies, and drugs. However, each of these applications may require different types of MNP tracers hence a careful selection of MNP design and coating is necessary to achieve outstanding results (Table 1). This section will focus on these biomedical applications and provide our insights on the suitable tracers for each application.

6.1. *In vivo* imaging

6.1.1. Vascular and perfusion imaging with MPI. MPI can deliver high quality images with no background signals, no penetration limit and high temporal resolution which makes it an ideal modality for real-time *in vivo* imaging of cardiovascular and cerebrovascular diseases. Recent studies also show that MPI can indicate any structural changes and allow for direct quantification of vascular stenosis for as small as 2 mm.[9] The key property for MNPs in *in vivo* imaging lies in their circulation time as it is vital for the MNPs to remain in the system for the whole imaging duration (usually can take from minutes up to hours). In a study conducted by Yu *et al.*, the potential of PEGylated SPIONs as a long circulating tracer (up to 140 min blood half-life) was highlighted as they that successfully allowed for the detection and quantification of gastrointestinal (GI) bleeding.[10] Furthermore, when Kaul *et al.* used LS-008, another SPION tracer coated with PEG polymer to study organ perfusion and angiography, it was shown that LS-008 has a better image resolution and longer blood half-life

Table 1 Summary of core materials and surface modifications with ideal properties for biomedical applications

Biomedical applications	Key criteria	Types of core materials	Surface modifications	Ref.
Vascular and perfusion imaging	• Long blood half-life • For neuroimaging, hydrodynamic size can't exceed 200 nm.	• Fe_3O_4 NPs • Metal ferrites • Fe@Fe_3O_4 • Maghemite NPs	• PEG coating • Red blood cells coating	5, 10, 156 and 158
Targeted imaging with MPI	• Long blood half-life • Need a proper targeting ligand conjugation	• FeCo@C • Fe_3O_4 NPs • Metal ferrites • Fe@Fe_3O_4	• PEG coating • Small molecules • Zwitterionic polymer	4, 12, 13 and 159
Therapeutic treatment using MPI	• Need a proper targeting ligand conjugation	• Fe_3O_4 NPs • Metal ferrites • Fe@Fe_3O_4 • FeCo alloy • Iron carbide	• DMSA coating (cancer treatment) • Biopolymer coating (drug delivery) • Silica coating (drug delivery)	13, 86, 130 and 137
Cellular tracking	• Long blood half-life • Positive surface charge	• Janus oxide • Cubic Fe_3O_4 NPs • Metal ferrite • Fe@Fe_3O_4	• Positive surface charge ligands • Biopolymer coating (*e.g.*, carboxymethyl chitosan and citric acid)	8, 14, 15 and 160–162
Thermal guided cancer therapy	• Wide coercive field • Hydrodynamic size: ≤100 nm • Suitable targeting ligand	• Hard metal ferrites (*e.g.*, $Co_xFe_{3-x}O_4$) • FeCO metal alloy • Cubic NPs (*e.g.*, $Zn_{0.4}Fe_{2.6}O_4$)	• Metallic coating (*e.g.*, Au) • Biomolecules coating for more uniform ablations	19, 20 and 164

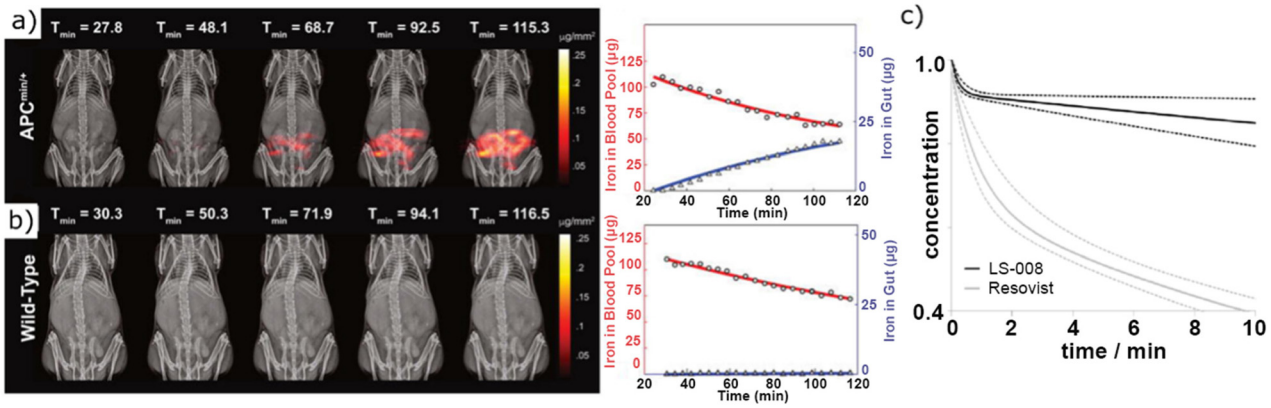

Fig. 11 APC $^{min/+}$ mouse was used as a disease model for GI bleeding. Representative subtracted MPI images of (a) an APC $^{min/+}$ mouse and (b) a wild-type mouse over a course of 117 min and the concentration of Fe in the blood pool (shown in red) and gut (shown in blue). The GI bleed can be visualised with high contrast in (a) for the diseased mouse model and none was observed in (b).[10] This figure has been reproduced from ref. 10 with permission from ACS Nano, copyright 2022. (c) The signal decay of LS-008 and Resovist® over time in the heart.[11] This figure has been reproduced from ref. 11 with permission from Physics in Medicine & Biology, copyright 2022.

than Resovist®.[11] After a few minutes of injection, the rate of blood clearance for Resovist® was determined to be much higher than that of LS-008 (Fig. 11). As a result, the majority of the Resovist® NPs were accumulated in the liver after 8 minutes of injection.[11] The MPI angiography images also demonstrated that LS-008 has a better delineation of visualised vessels (*i.e.*, caval veins, aorta and liver vasculature could be clearly distinguished) and showed no temporal fluctuation artifacts compared to Resovist®.[11]

Apart from cardiovascular imaging, MPI can also be used for the detection of ischemic stroke by acquiring images of cerebral perfusion. One of the risks for this type of cerebral assessment is the potential extravasation of MNP tracers into the brain parenchyma. This tracer extravasation will lead to many unwanted side effects from tracer deposition onto the central nervous system to contaminating the perfusion signal, which then results in incorrect reading of the cerebral blood volume.[156] In one study, Ludewig *et al.* assessed the potential of MPI for detecting acute stroke by using 65 nm LS-008 NPs. The study showed no signs of tracer extravasation in the brain parenchyma after 3 h of reperfusion and the stroke was also successfully detected in real time using MPI.[156] In addition, other studies also reported no tracer extravasation of SPIONs with hydrodynamic size of 50 nm and greater.[157]

It is worth noting that for neuroimaging, MNP tracers also need to be less than 200 nm in order to cross the blood brain barrier (BBB). Therefore, it is important to carefully choose the size of MNPs (*i.e.*, 50 nm – 200 nm) to avoid tracer extravasation and to successfully cross the BBB during cerebrovascular imaging. Furthermore, SPIONs can also be encapsulated in red blood cells (RBCs) to enhance their biocompatibility as well as prolonging their blood circulating time (*i.e.*, up to 12 days), which make these RBCs conjugated NPs ideal candidates for long term *in vivo* imaging applications.[5,158] Depending on duration of the applications, PEG polymer and RBCs coating can be used interchangeably for *in vivo* imaging.

6.1.2. Targeted Imaging with MPI. Targeted imaging has played a crucial role in the early detection and diagnosis of diseases including cancer. By conjugating SPIONs with an appropriate targeting ligand, MPI can offer many advantageous properties over the current modalities such as high sensitivity, high SNR, magnetic targeting and direct quantification of tumour mass.[5,12,16] Yu *et al.* was successfully using MPI to detect MDA-MB-231-luc xenograft tumours by intravenously injecting long circulating LS-008 tracers in tumour bearing rats.[5] Using lactoferrin, Arami *et al.* successfully showed a higher selectivity and accumulation rate of lactoferrin-conjugated MNPs at the brain tumour xenograft in mice compared unconjugated MNPs (Fig. 12).[4] Furthermore, by introducing a permanent magnet close to the tumour xenograft, a much higher accumulation of lactoferrin-conjugated MNPs was observed, hence allowing for another alternative targeting strategy using MPI.[4] In a different study, Jung *et al.* was able to monitor and track the SPIONs-labelled exosomes (*i.e.*, exosomes that were modified to carry SPIONs) *in vivo* to study the efficacy of these cell-derived vesicles toward hypoxic tumour *via* MPI.[12] The study also showed the potential of these exosomes for therapeutic treatment of cancer by loading drugs, such as Olaparib (a poly ADP ribose polymerase (PARP) inhibitor), into these vesicles and MPI can be used for the tracking in real time. However, conjugating nanoparticles with specific targeting ligand is not always mandatory. For example, in a recent study, Song *et al.*, was able to use MMPF NPs (iron oxide@semiconducting polymer Janus nanostructures) to target the orthotopic tumours in brain and breasts in mice. The results show that the MMPF NPs were able to diffuse into the brain tumour *via* enhanced permeability and retention (EPR) effect and can remain *in vivo* for up to 49 h after injection.[159]

Although Co is not typically employed *in vivo* due to toxicity concerns, effective coating that prevents Co leaching may make Co-containing MNPs viable options for MPI tracers. In a

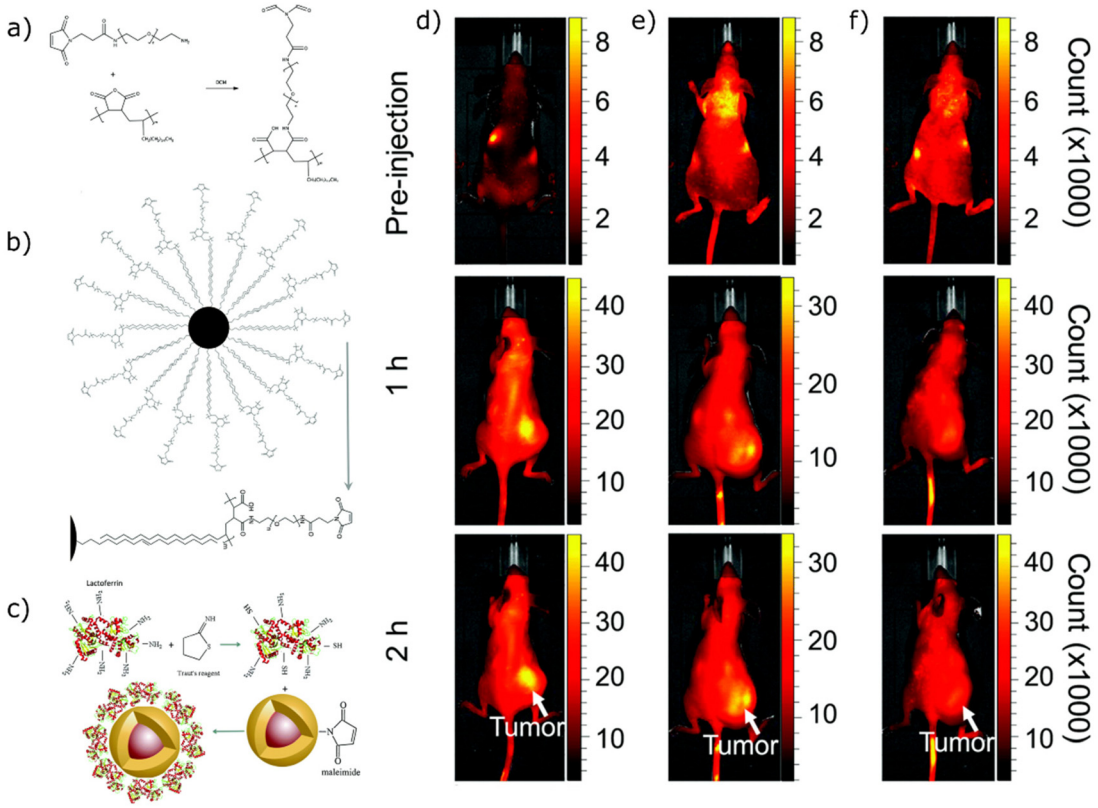

Fig. 12 Schematic illustration of surface functionalisation of NPs for glioma targeting studies. (a) Reaction between PEG polymer with PMAO to form PEG-PMAO copolymer with an active maleimide functional groups. (b) Surface functionalisation of magnetic nanoparticles with PEG-PMAO polymer to increase their water dispersity. (c) Conjugation of lactoferrin onto iron oxide nanoparticles using Traut's agent. Near *infra*-red fluorescence (NIRF) images of tumour xenograft bearing mice that was injected with Cy5.5-lactoferrin conjugated NPs (d) with and (e) without a permanent magnet placed on the right-side flank. (f) NIRF images of tumour xenograft bearing mice that was injected with Cy5.5 labelled NPs (lactoferrin free NPs) and without a permanent magnet.[4] This figure has been reproduced from ref. 4 with permission from Nanoscale, copyright 2022.

recent study, Song *et al.* successfully synthesised FeCo@C-PEG and showed that these NPs possessed 3.5 times greater MPI signal than that of Vivotrax for imaging of 4T1 breast tumours in living mice. In addition, the tumour uptake of these FeCo@C-PEG NPs was calculated to be higher than Vivotrax, which are 5.7% ID g^{-1} and 0.64% ID g^{-1} respectively after 24 h of injection; making these NPs more superior than commercial tracers for *in vivo* tumour imaging.[13] Therefore, it is important to choose an appropriate core and functionalise MNPs with a suitable biomarker for imaging of targeted sites and diseases.

6.2. Cellular tracking with MPI

Stem cell therapy has attracted great attention owing to their tissue regeneration potential, and ability to treat various diseases such as stroke, liver, heart failure and neurological diseases.[16,82] However, the biological fate of these administered stem cells is not fully understood. Thus, there is an opportunity for further investigation of their behaviour and migration pathways to diseased tissues *in vivo*. This can be achieved by using imaging modalities to track stem cells in biological environment. However, positron emission tomography (PET) and single-photon emission computed tomography (SPECT) were shown to be unsuitable for long term cellular tracking due to the use of radiotracers. This is because they have a relatively short half-life and can cause adverse effect on stem cell viability. In contrast, MPI uses non-toxic MNP tracers that can be tuned to possess long blood circulation time and high biocompatibility. Furthermore, owing to its quantitative nature and high contrast, MPI is a suitable imaging platform to track the fate of stem cells *in vivo*. By using MPI, Zheng *et al.* successfully monitored the *in vivo* distribution and clearance of human mesenchymal stem cells (hMSCs) by modifying them with Resovist®, a commercially available MPI tracer. These Resovist-labelled MSCs were initially localised in the lungs upon injection and the signals were visible for up to 12 days then were gradually cleared by the liver.[14] In another study, Zheng *et al.* further emphasised the potential of these SPIONs for long term cellular tracking, as the group successfully tracked and quantified these implanted Resovist-labelled neural progenitor cell (NPC) in rat brains for more than 3 months.[15]

In another study conducted by Song *et al.*, it was shown that 27 nm Janus MNPs (SPION-semiconducting polymer) can achieve 3-fold and 7-fold higher M_{sat} than the commercial tracers Vivotrax and Faraheme, respectively.[8] During *in vivo*

HeLa cell tracking, these Janus MNPs showed excellent MPI performance, low toxicity, and post-mortem analysis still displayed strong signal intensity even after 20 days of injection. Thus, Janus MNPs are great candidates for long term *in vivo* cell tracking.[8] Furthermore, by tuning the shape and size of SPIONs, Wang *et al.* was able to achieve a higher M_{sat} for 22 nm cubic iron oxide NPs (namely CIONs-22) at the same Fe content, which is 4.15-fold higher than that of Vivotrax.[16] By using these CIONs-22-labelled bone mesenchymal stem cells (BMSCs), Wang *et al.* also successfully monitored the migration and distribution patterns of these NPs toward the damaged tissues in ischemic mouse. In another study conducted by Rivera-Rodriguez *et al.*, it was shown that ferucarbotran (or Resovist®) could also be used to study the behaviour of adoptive cellular therapy (ACT) T cells *in vivo*.[17] However, the cellular uptake of these commercial tracers by ACT T cells was determined to be only 1 pg_{Fe} per cell, which is significantly lower when compared to other cells.

Since MPI tracers are mainly embedded into stem cells *via* endocytosis, the MNP properties such as surface charge, surface chemistry, and hydrodynamic size are highly important for an optimal internalisation.[160,161] In order to facilitate endocytosis, magnetic tracers are recommended to have a positive surface charge so they can be attracted to the negatively charged surface of cell membranes *via* electrostatic force. However, some studies have shown that surface coatings such as carboxymethyl chitosan and citric acid can increase the stem cell uptake of the MNPs despite the for stem cell uptake.[160–162] Therefore, a careful selection of size, surface charge and surface chemistry for MPI tracers is needed to achieve optimal results for cellular tracking applications.

6.3. Thermal guided cancer therapy with MPI

Hyperthermia therapy (HT), also known as thermal therapy, is a therapeutic method for cancer treatment that works by applying heat to a targeted region of the body. HT can also be used to sensitise tumours so that other treatments such as chemotherapy or radiotherapy can be more effective.[163] By utilising MNPs and an alternating magnetic field (AMF), magnetic hyperthermia (MHT) or magnetic fluid hyperthermia (MFH) can direct and ensure sufficient localisation of MNPs. However, MNPs can also accumulate in the off-target organs such as liver and spleen. Thus, the increase in temperature can induce collateral damage and necrosis in healthy tissues as well as changing their enzymatic behaviour.[163] In MHT, the heat induced is caused by the continuous magnetic relaxation of MNPs in an alternating field, which also relies on the same principle as MPI signal generation.[19] Therefore, if the AMF can be localised within the tumour only, damage on off-target organs can be avoided. Studies have shown that by adjusting the position of the field free region (FFR) in MPI, selective heating can be achieved and the tumour lesions could be ablated without harming nearby tissues.[18] Therefore, this makes MPI an ideal imaging platform in hyperthermia therapy to treat tumour with high precision.

For an optimal ablation of tumours, a more uniform distribution and penetration of MNPs into tumours is required. Studies have shown that by functionalising the surface of MNPs with a suitable targeting ligand such as CREKA (Cys-Arg-Glu-Lys-Ala), a penta-peptide that can target fibrin fibronectin complexes expressed by tumour cells in breast and interstitial cancer, it can promote a more uniform distribution of these conjugated NPs within 4T1-Luc breast cancer cells as revealed by both MPI and MRI imaging.[20] Apart from surface functionalisation, properties such as size, shape and composition of MNPs are also important to achieve outstanding results in hyperthermia. Studies have shown that MNPs of larger size are more preferrable to be used in hyperthermia treatment. This is because MNPs of larger size will be slightly ferrimagnetic and have a higher H_c and a higher remanent magnetisation (M_r) which are the important properties for MHT.[165] However, MNPs with very high H_c and M_r are also not suitable for MHT because they are unable to produce ideal specific heating power (SHP) and would require a higher magnetic field strength to be excited.[165] Furthermore, ferrimagnetic NPs also adversely affect MPI signalling due to a slower magnetic relaxation which results in poorer image resolution. Additionally, if the NPs become too small, H_c value would be negligible hence also not suitable to be used in magnetic hyperthermia. As a result, magnetite of 10 nm was shown to not be desirable as hyperthermia agents.[74] Therefore, it is critical to carefully control the size of MNPs so that it can behave like a soft magnet and generate exceptional SHP value while still maintaining good MPI signal. Apart from size, shape also play a key role in achieving excellent performance in MHT.

Studies have shown that cubic MNPs possess a higher shape anisotropy compared to their spherical counterparts hence a study conducted by Reyes-Ortega *et al.*, it is found that 24 nm cuboidal SPIONs demonstrated an improved performance in hyperthermia compared to spherical and rod-shaped SPIONs (Fig. 13a).[164] Though, all three SPIONs can increase the solution temperature from ambient value to 45 °C within a minute, cuboidal NPs still achieved the maximum heating value (Fig. 13b).[164] However, due to the higher value of H_c, these cubic NPs are not ideal as MPI tracers. In order to overcome this issue, SPIONs have been doped with various metals to tune their magnetic properties so that these tracers can be used for a wide range of applications, specifically hyperthermia. In a study conducted by Bauer *et al.*, it is shown that by doping cubic SPIONs with 13% zinc can effectively increase their M_{sat} value while still maintaining their excellent MHT performance.[19] These cubic zinc ferrite ($Zn_{0.4}Fe_{2.6}O_4$) NPs exhibited a 2-fold enhancement in SNR compared to undoped counterparts which enabled their use as MPI tracers.[19] Furthermore, these cubic NPs also demonstrated an improvement in hyperthermia performance compared to current commercial tracers (*i.e.*, higher SNR value and 5-fold enhancement in specific absorption rate over spherical NPs).[19] Therefore, with the improved magnetic properties and excellent heating efficiency, this makes these cubic zinc ferrite NPs ideal candidates to be used in MPI coupled with hyperthermia treatment.

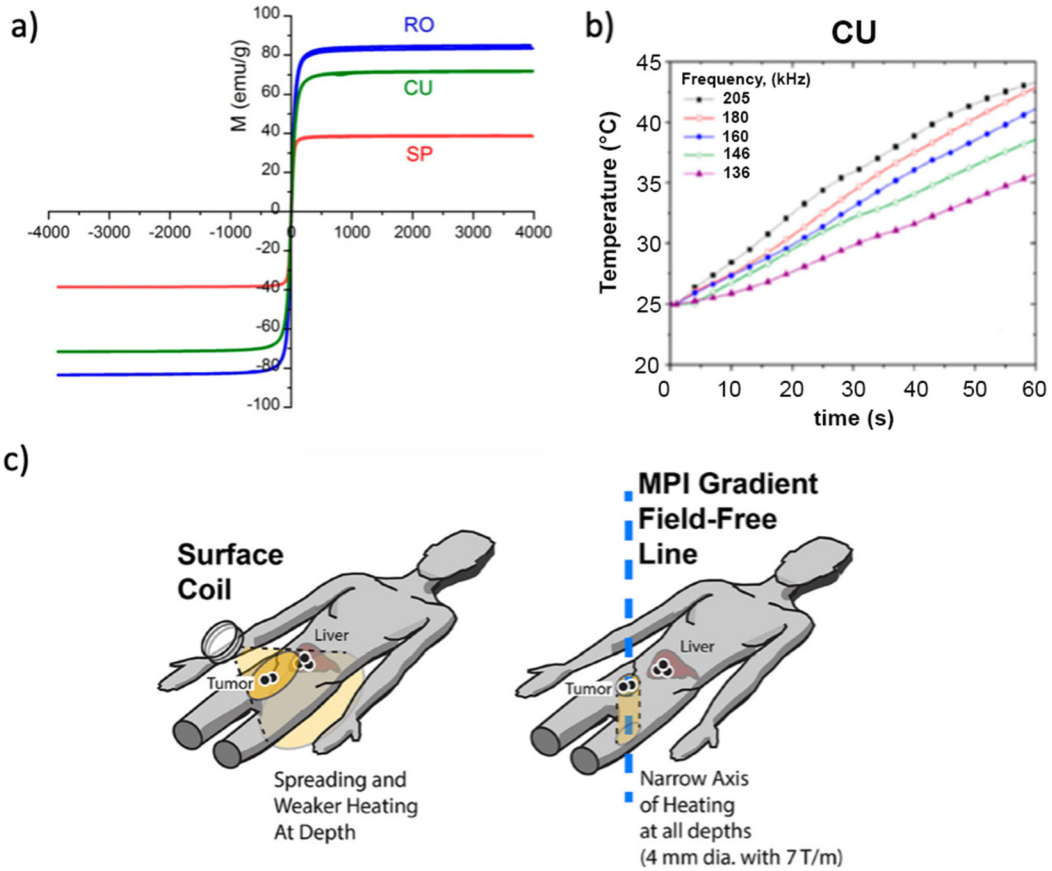

Fig. 13 (a) Magnetisation curve at 25 °C of nanorods (RO), nanocubes (CU) and nanospheres (SP). Inset: low – field detail. (b) Hyperthermia response tests: temperature–time curve of CU at different field frequencies and 16.2 kA m^{-1} field strength.[164] This figure has been reproduced from ref. 164 with permission from Nanomaterials, copyright 2022. (c) Scheme illustrating the potential of MPI for hyperthermia treatment with high precision.[18] This figure has been reproduced from ref. 18 with permission from ACS Nano, copyright 2022.

Furthermore, a study conducted by Joshi *et al.*, found that doping SPIONs with cobalt also resulted in an increase in coercive fields hence higher heat dissipations.[165] However, some studies also shown that cobalt ferrite NPs with a $CoFe_2O_4$ composition of 10 nm–15 nm are not suitable to be used in hyperthermia due to an extremely high value of H_c[165] However, studies have shown that by tuning the composition of cobalt in iron oxide NPs can successfully reduce the H_c value. In a study conducted by Dutz *et al.*, it is demonstrated that cobalt ferrite that contains 6.4%, 8.6% and 12.6% of cobalt maximised the SHP value at low, medium and high magnetic field strength respectively.[74] Furthermore, these cobalt ferrite NPs also exhibited high M_{sat} and had excellent thermal and chemical stabilities.[166,167] Therefore, if the correct composition of Co is used, cobalt doped SPIONs can be ideal MPI tracers for MHT.

In summary, MNP materials such as cube-shaped zinc ferrite NPs and cobalt ferrite NPs are excellent candidates for magnetic hyperthermia therapy using MPI. In terms of surface modification, metallic coating is preferred due to high conductivity which can minimise the amount heat loss compared to organic coatings. Although, as discussed earlier, functionalising MNPs with biomolecules can also facilitate the uptake of these tracers and optimise their distribution for a more uniform tumour ablation. Therefore, it is necessary to carefully consider the advantages and disadvantages of each MNP and coating for exceptional results in MHT using MPI.

7. Conclusion and future opportunities

This review paper focussed on different MNPs including magnetite, metal ferrites, maghemite, and zero valent Fe@Fe_3O_4, iron carbide and iron–cobalt alloy NPs that can potentially be used as MPI tracers. We provided our insights on what would be perceived as the "best" core material and the synthetic routes for each material was also discussed. Properties such as superparamagnetism, short magnetic relaxation, and size of nanoparticles play an important role in MPI signal generation and must be carefully considered to achieve the best results. We also highlighted the importance of surface modifications in improving the functionality of MNPs for a wide range of biomedical applications in MPI. Applications including *in vivo*

imaging, cellular tracking, and hyperthermia were briefly discussed and we have also presented our insights on what would be the ideal material for each of these applications.

This review highlights the major advantages of MPI for different biomedical applications and how magnetic nanoparticles are tailored for each of these applications. These advantages allow for exciting opportunities for future directions in the field on MPI research. For example, the key properties of MNPs for more specific applications such as leukemia studies have not yet been fully explored. Hence, there is an unmet need to investigate the ideal size and coating that would be best fitted for each application for MPI to be used clinically. Furthermore, there is also an opportunity to explore other coating options to improve the circulation time and biodistribution of administered NPs *in vivo*. Additionally, properties such as superparamagnetism, short magnetic relaxation, high M_{sat}, and the size of nanoparticles of MNPs need to be tailored for specific applications. Thus, despite major advances in the field, there is still potential for further research to create and understand MNP tracers that can be implemented for MPI in clinical applications.

Conflicts of interest

There are no conflicts to declare.

References

1 P. M. Ferguson, K. W. Feindel, A. Slocombe, M. MacKay, T. Wignall, B. Delahunt, R. D. Tilley and I. F. Hermans, *PLoS One*, 2013, **8**, 1–7.
2 H. Arami, A. P. Khandhar, A. Tomitaka, E. Yu, P. W. Goodwill, S. M. Conolly and K. M. Krishnan, *Biomaterials*, 2015, **52**, 251–261.
3 Q. Gao, L. Yan, M. Chiorazzo, E. James Delikatny, A. Tsourkas and Z. Cheng, *Chem. Commun.*, 2015, **51**, 12313–12315.
4 H. Arami, E. Teeman, A. Troksa, H. Bradshaw, K. Saatchi, A. Tomitaka, S. S. Gambhir, U. O. Häfeli, D. Liggitt and K. M. Krishnan, *Nanoscale*, 2017, **9**, 18723–18730.
5 E. Y. Yu, M. Bishop, B. Zheng, R. M. Ferguson, A. P. Khandhar, S. J. Kemp, K. M. Krishnan, P. W. Goodwill and S. M. Conolly, *Nano Lett.*, 2017, **17**, 1648–1654.
6 A. P. Khandhar, R. M. Ferguson, H. Arami and K. M. Krishnan, *Biomaterials*, 2013, **34**, 3837–3845.
7 B. Gleich and J. Weizenecker, *Nature*, 2005, **435**, 1214–1217.
8 G. Song, M. Chen, Y. Zhang, L. Cui, H. Qu, X. Zheng, M. Wintermark, Z. Liu and J. Rao, *Nano Lett.*, 2018, **18**, 182–189.
9 S. Vaalma, J. Rahmer, N. Panagiotopoulos, R. L. Duschka, J. Borgert, J. Barkhausen, F. M. Vogt and J. Haegele, *PLoS One*, 2017, **12**, 1–22.
10 E. Y. Yu, P. Chandrasekharan, R. Berzon, Z. W. Tay, X. Y. Zhou, A. P. Khandhar, R. M. Ferguson, S. J. Kemp, B. Zheng, P. W. Goodwill, M. F. Wendland, K. M. Krishnan, S. Behr, J. Carter and S. M. Conolly, *ACS Nano*, 2017, **11**, 12067–12076.
11 M. G. Kaul, T. Mummert, C. Jung, J. Salamon, A. P. Khandhar, K. M. Krishnan, G. Adam and T. Knopp, *Phys. Med. Biol.*, 2017, **69**, 3454–3469.
12 K. O. Jung, H. Jo, J. H. Yu, S. S. Gambhir and G. Pratx, *Biomaterials*, 2018, **177**, 139–148.
13 G. Song, M. Kenney, Y. S. Chen, X. Zheng, Y. Deng, Z. Chen, S. X. Wang, S. S. Gambhir, H. Dai and J. Rao, *Nat. Biomed. Eng.*, 2020, **4**, 325–334.
14 B. Zheng, M. P. Von See, E. Yu, B. Gunel, K. Lu, T. Vazin, D. V. Schaffer, P. W. Goodwill and S. M. Conolly, *Theranostics*, 2016, **6**, 291–301.
15 B. Zheng, T. Vazin, P. W. Goodwill, A. Conway, A. Verma, E. Ulku Saritas, D. Schaffer and S. M. Conolly, *Sci. Rep.*, 2015, **5**, 1–9.
16 Q. Wang, X. Ma, H. Liao, Z. Liang, F. Li, J. Tian and D. Ling, *ACS Nano*, 2020, **14**, 2053–2062.
17 A. Rivera-Rodriguez, L. B. Hoang-Minh, A. Chiu-Lam, N. Sarna, L. Marrero-Morales, D. A. Mitchell and C. M. Rinaldi-Ramos, *Nanotheranostics*, 2021, **5**, 431–444.
18 Z. W. Tay, P. Chandrasekharan, A. Chiu-Lam, D. W. Hensley, R. Dhavalikar, X. Y. Zhou, E. Y. Yu, P. W. Goodwill, B. Zheng, C. Rinaldi and S. M. Conolly, *ACS Nano*, 2018, **12**, 3699–3713.
19 L. M. Bauer, S. F. Situ, M. A. Griswold and A. C. S. Samia, *Nanoscale*, 2016, **8**, 12162–12169.
20 Y. Du, X. Liu, Q. Liang, X. J. Liang and J. Tian, *Nano Lett.*, 2019, **19**, 3618–3626.
21 I. Francolini, M. Palombo, G. Casini, L. D'Ilario, A. Martinelli, V. Rinaldelli and A. Piozzi, *J. Controlled Release*, 2010, **148**, e57–e59.
22 E. L. S. Wong and J. J. Gooding, *Anal. Chem.*, 2006, **78**, 2138–2144.
23 D. Chen, Y. Wu, S. Hoque, R. D. Tilley and J. J. Gooding, *Chem. Sci.*, 2021, **12**, 5196–5201.
24 M. Mehdipour, L. Gloag, D. T. Bennett, S. Hoque, R. Pardehkhorram, P. Bakthavathsalam, V. R. Gonçales, R. D. Tilley and J. J. Gooding, *J. Mater. Chem. C*, 2021, **9**, 1034–1043.
25 L. Gloag, M. Mehdipour, D. Chen, R. D. Tilley and J. J. Gooding, *Adv. Mater.*, 2019, **31**, 1–26.
26 L. Gloag, M. Mehdipour, M. Ulanova, K. Mariandry, M. A. Nichol, D. J. Hernández-Castillo, J. Gaudet, R. Qiao, J. Zhang, M. Nelson, B. Thierry, M. A. Alvarez-Lemus, T. T. Tan, J. J. Gooding, N. Braidy, P. S. Sachdev and R. D. Tilley, *Chem. Commun.*, 2020, **56**, 3504–3507.
27 C. Shasha, E. Teeman and K. M. Krishnan, *Biomed. Phys. Eng. Express*, 2019, **5**, 055–010.
28 J. Landers, S. Salamon, H. Remmer, F. Ludwig and H. Wende, *Nano Lett.*, 2016, **16**, 1150–1155.
29 J. P. Fortin, F. Gazeau and C. Wilhelm, *Eur. Biophys. J.*, 2008, **37**, 223–228.

30 S. A. Kahani and Z. Yagini, *Bioinorg. Chem. Appl.*, 2014, **2014**, 384984.
31 A. G. Kolhatkar, A. C. Jamison, D. Litvinov, R. C. Willson and T. R. Lee, *Tuning the magnetic properties of nanoparticles*, 2013, vol. 14.
32 Q. Li, C. W. Kartikowati, S. Horie, T. Ogi, T. Iwaki and K. Okuyama, *Sci. Rep.*, 2017, **7**, 1–4.
33 R. M. Ferguson, K. R. Minard, A. P. Khandhar and K. M. Krishnan, *Med. Phys.*, 2011, **38**, 1619–1626.
34 P. Chandrasekharan, Z. W. Tay, X. Y. Zhou, E. Yu, R. Orendorff, D. Hensley, Q. Huynh, K. L. B. Fung, C. C. Vanhook, P. Goodwill, B. Zheng and S. Conolly, *A perspective on a rapid and radiation-free tracer imaging modality, magnetic particle imaging, with promise for clinical translation*, 2018, vol. 91.
35 S. Mukherjee, L. Liang and O. Veiseh, *Pharmaceutics*, 2020, **12**, 147.
36 Y. Bao, T. Wen, A. C. S. Samia, A. Khandhar and K. M. Krishnan, *J. Mater. Sci.*, 2016, **51**, 513–553.
37 M. G. Miguel, J. P. Lourenço and M. L. Faleiro, *Int. J. Mol. Sci.*, 2020, **21**, 1–24.
38 N. Lee and T. Hyeon, *Chem. Soc. Rev.*, 2012, **41**, 2575–2589.
39 K. Reczyńska, M. Marszałek, A. Zarzycki, W. Reczyński, K. Kornaus, E. Pamuła and W. Chrzanowski, *Nanomaterials*, 2020, **10**, 1076.
40 Y. Lu, A. Rivera-Rodriguez, Z. W. Tay, D. Hensley, K. L. B. Fung, C. Colson, C. Saayujya, Q. Huynh, L. Kabuli, B. Fellows, P. Chandrasekharan, C. Rinaldi and S. Conolly, *Int. J. Hyperthermia*, 2020, **37**, 141–154.
41 C. Billings, M. Langley, G. Warrington, F. Mashali and J. A. Johnson, *Int. J. Mol. Sci.*, 2021, **22**, 7651.
42 G. C. Bleier, J. Watt, C. K. Simocko, J. M. Lavin and D. L. Huber, *Angew. Chem., Int. Ed.*, 2018, **57**, 7678–7681.
43 J. Wallyn, N. Anton and T. F. Vandamme, *Pharmaceutics*, 2019, **11**, 1–29.
44 Q. Yang, Y. Dong, Y. Qiu, X. Yang, H. Cao and Y. Wu, *Colloids Surf., B*, 2020, **191**, 111014.
45 R. Hufschmid, J. Landers, C. Shasha, S. Salamon, H. Wende and K. M. Krishnan, *Phys. Status Solidi A*, 2019, **216**, 1–8.
46 X. Han, Y. Li, W. Liu, X. Chen, Z. Song, X. Wang, Y. Deng, X. Tang and Z. Jiang, *Diagnostics*, 2020, **10**, 1–12.
47 J. Haegele, R. L. Duschka, M. Graeser, C. Schaecke, N. Panagiotopoulos, K. Lüdtke-Buzug, T. M. Buzug, J. Barkhausen and F. M. Vogt, *Int. J. Nanomed.*, 2014, **9**, 4203–4209.
48 Z. Jiang, X. Han, Y. Du, Y. Li, Y. Li, J. Li, J. Tian and A. Wu, *Nano Lett.*, 2021, **21**, 2730–2737.
49 R. M. Ferguson, A. P. Khandhar, S. J. Kemp, H. Arami, E. U. Saritas, L. R. Croft, J. Konkle, P. W. Goodwill, A. Halkola, J. Rahmer, J. Borgert, S. M. Conolly and K. M. Krishnan, *IEEE Trans Med Imaging*, 2015, **34**, 1077–1084.
50 A. Antonelli, P. Szwargulski, E. S. Scarpa, C. Grüttner, L. Guidi, G. Ambrosi, T. Knopp and M. Magnani, *Int. J. Magn. Part. Imaging*, 2020, **6**, 1–3.
51 A. Antonelli, P. Szwargulski, E. S. Scarpa, F. Thieben, G. Cordula, G. Ambrosi, L. Guidi, P. Ludewig, T. Knopp and M. Magnani, *Nanomedicine*, 2020, **15**, 739–753.
52 P. Vogel, T. Kampf, M. A. Rückert, C. Grüttner, A. Kowalski, H. Teller and V. C. Behr, *Int. J. Magn. Part. Imaging*, 2021, 7(1), DOI: **10.18416/IJMPI.2021.2103003**.
53 N. Panagiotopoulos, R. L. Duschka, M. Ahlborg, G. Bringout, C. Debbeler, M. Graeser, C. Kaethner, K. Lüdtke-Buzug, H. Medimagh, J. Stelzner, T. M. Buzug, J. Barkhausen, F. M. Vogt and J. Haegele, *Int. J. Nanomed. Dovepress*, 2015, 10–3097.
54 P. Reimer and T. Balzer, *Eur. Radiol.*, 2003, **13**, 1266–1276.
55 E. Kim, J. M. Kim, L. Kim, S. J. Choi, I. S. Park, J. Y. Han, Y. C. Chu, E. S. Choi, K. Na and S. S. Hon, *Int. J. Nanomed.*, 2016, **11**, 4595–4607.
56 D. Eberbeck, F. Wiekhorst, S. Wagner and L. Trahms, *Appl. Phys. Lett.*, 2011, **98**, 1–4.
57 D. Kokuryo, Y. Anraku, A. Kishimura, S. Tanaka, M. R. Kano, J. Kershaw, N. Nishiyama, T. Saga, I. Aoki and K. Kataoka, *J. Controlled Release*, 2013, **169**, 220–227.
58 S. J. Kemp, R. M. Ferguson, A. P. Khandhar and K. M. Krishnan, *RSC Adv.*, 2016, **6**, 77452–77464.
59 R. Hufschmid, H. Arami, R. M. Ferguson, M. Gonzales, E. Teeman, L. N. Brush, N. D. Browning and K. M. Krishnan, *Nanoscale*, 2015, **7**, 11142–11154.
60 S. A. Shah, D. B. Reeves, R. M. Ferguson, J. B. Weaver and K. M. Krishnan, *Phys. Rev. B: Condens. Matter Mater. Phys.*, 2015, **92**, 094438.
61 V. Herynek, M. Babič, O. Kaman, H. Charvátová, M. Veselá and L. Šefc, *J. Nanopart. Res.*, 2021, **52**, 1–15.
62 M. L. Aparna, A. N. Grace, P. Sathyanarayanan and N. K. Sahu, *J. Alloys Compd.*, 2018, **745**, 385–395.
63 T. Tangcharoen, A. Ruangphanit and W. Pecharapa, *Ceram. Int.*, 2013, **39**, S239–S243.
64 B. Süngü Mısırlıoğlu, Ö. Çakır, H. Calik and R. Cakir-Koc, *Inorg. Nano-Met. Chem.*, 2022, **52**, 57–62.
65 O. Kaman, D. Kubániová, K. Knížek, L. Kubíčková, M. Klementová, J. Kohout and Z. Jirák, *J. Alloys Compd.*, 2021, **888**, 161471.
66 T. Tangcharoen, A. Ruangphanit and W. Pecharapa, *Ceram. Int.*, 2013, **39**, S239–S243.
67 J. H. Lee, Y. M. Huh, Y. W. Jun, J. W. Seo, J. T. Jang, H. T. Song, S. Kim, E. J. Cho, H. G. Yoon, J. S. Suh and J. Cheon, *Nat. Med.*, 2007, **13**, 95–99.
68 Y. W. Jun, J. H. Lee and J. Cheon, *Angew. Chem., Int. Ed.*, 2008, **47**, 5122–5135.
69 K. Zipare, J. Dhumal, S. Bandgar, V. Mathe and G. Shahane, *J. Nanosci., NanoEng. Appl.*, 2015, **1**, 178–182.
70 A. R. O. Rodrigues, J. M. F. Ramos, I. T. Gomes, B. G. Almeida, J. P. Araújo, M. J. R. P. Queiroz, P. J. G. Coutinho and E. M. S. Castanheira, *RSC Adv.*, 2016, **6**, 17302–17313.
71 B. Sahoo, K. S. P. Devi, S. Dutta, T. K. Maiti, P. Pramanik and D. Dhara, *J. Colloid Interface Sci.*, 2014, **431**, 31–41.

72 M. Goodarz Naseri, E. Bin Saion, H. A. Ahangar, M. Hashim and A. H. Shaari, *J. Magn. Magn. Mater.*, 2011, **323**, 1745–1749.
73 Y. Miao, Q. Xie, H. Zhang, J. Cai, X. Liu, J. Jiao, S. Hu, A. Ghosal, Y. Yang and H. Fan, *Theranostics*, 2019, **9**, 1764–1776.
74 S. Dutz, N. Buske, J. Landers, C. Gräfe, H. Wende and J. H. Clement, *Nanomaterials*, 2020, **10**, 1019.
75 M. Irfan, N. Dogan, A. Bingolbali and F. Aliew, *J. Magn. Magn. Mater.*, 2021, **537**, 168150.
76 I. J. Bruce, J. Taylor, M. Todd, M. J. Davies, E. Borioni, C. Sangregorio and T. Sen, *J. Magn. Magn. Mater.*, 2004, **284**, 145–160.
77 R. L. Rebodos and P. J. Vikesland, *Langmuir*, 2010, **26**, 16745–16753.
78 H. Liang, X. Wu, G. Zhao, K. Feng, K. Ni and X. Sun, *J. Am. Chem. Soc.*, 2021, **143**, 15812–15823.
79 U. Jeong, X. Teng, Y. Wang, H. Yang and Y. Xia, *Adv. Mater.*, 2007, **19**, 33–60.
80 S. Cheong, P. Ferguson, I. F. Hermans, G. N. L. Jameson, S. Prabakar, D. A. J. Herman and R. D. Tilley, *ChemPlusChem*, 2012, **77**, 135–140.
81 A. J. McGrath, S. Cheong, A. M. Henning, J. J. Gooding and R. D. Tilley, *Chem. Commun.*, 2017, **53**, 11548–11551.
82 C. Lu, L. Han, J. Wang, J. Wan, G. Song and J. Rao, *Chem. Soc. Rev.*, 2021, **50**, 8102–8146.
83 C. M. Wang, D. R. Baer, L. E. Thomas, J. E. Amonette, J. Antony, Y. Qiang and G. Duscher, *J. Appl. Phys.*, 2005, **98**, 094308.
84 S. Cheong, P. Ferguson, K. W. Feindel, I. F. Hermans, P. T. Callaghan, C. Meyer, A. Slocombe, C. H. Su, F. Y. Cheng, C. S. Yeh, B. Ingham, M. F. Toney and R. D. Tilley, *Angew. Chem., Int. Ed.*, 2011, **50**, 4206–4209.
85 L. Gloag, M. Mehdipour, D. Chen, R. D. Tilley and J. J. Gooding, *Adv. Mater.*, 2019, **31**, 1–26.
86 J. Yu, C. Yang, J. Li, Y. Ding, L. Zhang, M. Z. Yousaf, J. Lin, R. Pang, L. Wei, L. Xu, F. Sheng, C. Li, G. Li, L. Zhao and Y. Hou, *Adv. Mater.*, 2014, **26**, 4114–4120.
87 W. S. Seo, J. H. Lee, X. Sun, Y. Suzuki, D. Mann, Z. Liu, M. Terashima, P. C. Yang, M. V. McConnell, D. G. Nishimura and H. Dai, *Nat. Mater.*, 2006, **5**, 971–976.
88 A. G. Roca, L. Gutiérrez, H. Gavilán, M. E. Fortes Brollo, S. Veintemillas-Verdaguer and M. del P. Morales, *Adv. Drug Delivery Rev.*, 2019, **138**, 68–104.
89 N.-L. Wu, *et al.*, *Mater. Chem.*, 2003, **126**, 273–279.
90 E. C. Vreeland, J. Watt, G. B. Schober, B. G. Hance, M. J. Austin, A. D. Price, B. D. Fellows, T. C. Monson, N. S. Hudak, L. Maldonado-Camargo, A. C. Bohorquez, C. Rinaldi and D. L. Huber, *Chem. Mater.*, 2015, **27**, 6059–6066.
91 G. K. Soon, Y. Piao, J. Park, S. Angappane, Y. Jo, N. M. Hwang, J. G. Park and T. Hyeon, *J. Am. Chem. Soc.*, 2007, **129**, 12571–12584.
92 H. Rashid, M. A. Mansoor, B. Haider, R. Nasir, S. B. Abd Hamid and A. Abdulrahman, *Sep. Sci. Technol.*, 2020, **55**, 1207–1215.
93 M. Zia, A. R. Phull and J. S. Ali, *Nanotechnol., Sci. Appl.*, 2016, 49–67.
94 J. Mahin, C. O. Franck, L. Fanslau, H. K. Patra, M. Mantle, L. Fruk and L. Torrente-Murciano, *React. Chem. Eng.*, 2021, **6**, 1961–1973.
95 K. Woo, J. Hong, S. Choi, H. Lee, J. Ahn, C. S. Kim and S. W. Lee, *Chem. Mater.*, 2004, **16**, 2814–2818.
96 L. L. Israel, A. Galstyan, E. Holler and J. Y. Ljubimova, *J. Controlled Release*, 2020, **320**, 45–62.
97 M. I. Dar and S. A. Shivashankar, *RSC Adv.*, 2014, **4**, 4105–4113.
98 T. Hyeon, Su S. Lee, J. Park, Y. Chung and H. B. Na, *J. Am. Chem. Soc.*, 2001, **123**, 12798–12801.
99 S. Peng, C. Wang, J. Xie and S. Sun, *J. Am. Chem. Soc.*, 2006, 10676–10677.
100 M. Unni, A. M. Uhl, S. Savliwala, B. H. Savitzky, R. Dhavalikar, N. Garraud, D. P. Arnold, L. F. Kourkoutis, J. S. Andrew and C. Rinaldi, *ACS Nano*, 2017, **11**, 2284–2303.
101 J. Park, E. Lee, N. M. Hwang, M. Kang, C. K. Sung, Y. Hwang, J. G. Park, H. J. Noh, J. Y. Kim, J. H. Park and T. Hyeon, *Angew. Chem., Int. Ed.*, 2005, **44**, 2872–2877.
102 K. K. Kefeni, T. A. M. Msagati, T. T. I. Nkambule and B. B. Mamba, *J. Environ. Chem. Eng.*, 2018, **6**, 1865–1874.
103 W. Karim, A. Kleibert, U. Hartfelder, A. Balan, J. Gobrecht, J. A. van Bokhoven and Y. Ekinci, *Sci. Rep.*, 2016, **6**, 18818.
104 S. P. Schwaminger, C. Syhr and S. Berensmeier, *Crystals*, 2020, **10**, 1–12.
105 B. H. Kim, N. Lee, H. Kim, K. An, Y. Il Park, Y. Choi, K. Shin, Y. Lee, S. G. Kwon, H. Bin Na, J.-G. Park, T.-Y. Ahn, Y.-W. Kim, W. K. Moon, S. H. Choi and T. Hyeon, *J. Am. Chem. Soc.*, 2011, **133**, 12624–12631.
106 X. Teng and H. Yang, *J. Mater. Chem.*, 2004, **14**, 774–779.
107 P. Cheah, J. Qu, Y. Li, D. Cao, X. Zhu and Y. Zhao, *J. Magn. Magn. Mater.*, 2021, **540**, 168481.
108 S. Sun and H. Zeng, *J. Am. Chem. Soc.*, 2002, **124**, 8204–8205.
109 J. Yang, Q. Kou, Y. Liu, D. Wang, Z. Lu, L. Chen, Y. Zhang, Y. Wang, Y. Zhang, D. Han and S. G. Xing, *Powder Technol.*, 2017, **319**, 53–59.
110 L. T. Lu, N. T. Dung, L. D. Tung, C. T. Thanh, O. K. Quy, N. V. Chuc, S. Maenosono and N. T. K. Thanh, *Nanoscale*, 2015, **7**, 19596–19610.
111 L. Zhang, R. He and H.-C. Gu, *Appl. Surf. Sci.*, 2006, **253**, 2611–2617.
112 D. Wilson and M. A. Langell, *Appl. Surf. Sci.*, 2014, **303**, 6–13.
113 C. Moya, X. Batlle and A. Labarta, *Phys. Chem. Chem. Phys.*, 2015, **17**, 27373–27379.
114 M. Yin, A. Willis, F. Redl, N. J. Turro and S. P. O'Brien, *J. Mater. Res.*, 2004, **19**, 1208–1215.
115 M. Filippousi, M. Angelakeris, M. Katsikini, E. Paloura, I. Efthimiopoulos, Y. Wang, D. Zamboulis and G. Van Tendeloo, *J. Phys. Chem. C*, 2014, **118**, 16209–16217.
116 M. Nadeem, M. Ahmad, M. S. Akhtar, A. Shaari, S. Riaz, S. Naseem, M. Masood and M. A. Saeed, *PLoS One*, 2016, **11**, e0158084.

117 D. Li, S. J. Li, Y. Zhang, J. J. Jiang, W. J. Gong, J. H. Wang and Z. D. Zhang, *Mater. Res. Innovations*, 2015, **19**, S58–S62.
118 A. J. McGrath, S. Cheong, A. M. Henning, J. J. Gooding and R. D. Tilley, *Chem. Commun.*, 2017, **53**, 11548–11551.
119 J. Weizenecker, B. Gleich, J. Rahmer and J. Borgert, *Phys. Med. Biol.*, 2012, **57**, 7317–7327.
120 R. M. Cornell and U. Schwertman, *The Iron Oxides: Structure, Properties, Reactions, Occurences and Uses*, 2nd end, 2003.
121 M. O. Rigo and J. Kleinclauss, *IEEE Trans. Magn.*, 2017, **53**, 1–4.
122 G. Cotin, C. Kiefer, F. Perton, D. Ihiawakrim, C. Blanco-Andujar, S. Moldovan, C. Lefevre, O. Ersen, B. Pichon, D. Mertz and S. Bégin-Colin, *Nanomaterials*, 2018, **8**, 1–16.
123 G. Cotin, C. Blanco-Andujar, F. Perton, L. Asín, J. M. de la Fuente, W. Reichardt, D. Schaffner, D.-V. Ngyen, D. Mertz, C. Kiefer, F. Meyer, S. Spassov, O. Ersen, M. Chatzidakis, G. A. Botton, C. Hénoumont, S. Laurent, J.-M. Greneche, F. J. Teran, D. Ortega, D. Felder-Flesch and S. Begin-Colin, *Nanoscale*, 2021, **13**, 14552–14571.
124 M. V. Kovalenko, M. I. Bodnarchuk, R. T. Lechner, G. Hesser, F. Schäffler and W. Heiss, *J. Am. Chem. Soc.*, 2007, **129**, 6352–6353.
125 A. J. McGrath, C. Dolan, S. Cheong, D. A. J. Herman, B. Naysmith, F. Zong, P. Galvosas, K. J. Farrand, I. F. Hermans, M. Brimble, D. E. Williams, J. Jin and R. D. Tilley, *J. Magn. Magn. Mater.*, 2017, **439**, 251–258.
126 J. Zhang and W. Marksaltzman, *Chem. Eng. Prog.*, 2013, **109**, 25–30.
127 Z. Liu, C. Davis, W. Cai, L. He, X. Chen and H. Dai, *Proc. Natl. Acad. Sci. U. S. A.*, 2008, **105**, 1410–1415.
128 Y. Li, M. Kröger and W. K. Liu, *Nanoscale*, 2015, **7**, 16631–16646.
129 E. S. Martins, A. Espindola, T. N. Britos, C. Chagas, E. Barbosa, C. E. Castro, F. L. A. Fonseca and P. S. Haddad, *ChemistrySelect*, 2021, **6**, 7931–7935.
130 S. Çitoğlu, Ö. D. Coşkun, L. D. Tung, M. A. Onur and N. T. Kim Thanh, *Nanomedicine*, 2021, **16**, 925–941.
131 Y. Liu and J. Wang, *Toxicol. Sci.*, 2013, **131**, 521–536.
132 L. Li, K. Y. Mak, C. W. Leung, K. Y. Chan, W. K. Chan, W. Zhong and P. W. T. Pong, *Microelectron. Eng.*, 2013, **110**, 329–334.
133 J. Ding, K. Tao, J. Li, S. Song and K. Sun, *Colloids Surf., B*, 2010, **79**, 184–190.
134 H. Kratz, M. Taupitz, A. A. De Schellenberger, O. Kosch, D. Eberbeck, S. Wagner, L. Trahms, B. Hamm and J. Schnorr, *PLoS One*, 2018, **13**, 1–22.
135 K. Vasić, Ž. Knez, E. A. Konstantinova, A. I. Kokorin, S. Gyergyek and M. Leitgeb, *React. Funct. Polym.*, 2020, **148**, 104481.
136 N. O. Fowler and J. C. Holmes, *Am. Heart J.*, 1964, **68**, 204–213.
137 R. P. Dhavale, R. P. Dhavale, S. C. Sahoo, P. Kollu, S. U. Jadhav, P. S. Patil, T. D. Dongale, A. D. Chougale and P. B. Patil, *J. Phys. Chem. Solids*, 2021, **148**, 109749.
138 E. H. Kim, H. S. Lee, B. K. Kwak and B. K. Kim, *J. Magn. Magn. Mater.*, 2005, **289**, 328–330.
139 J. L. Arias, L. H. Reddy and P. Couvreur, *J. Mater. Chem.*, 2012, **22**, 7622–7632.
140 A. P. Khandhar, P. Keselman, S. J. Kemp, R. M. Ferguson, P. W. Goodwill, S. M. Conolly and K. M. Krishnan, *Nanoscale*, 2017, **9**, 1299–1306.
141 H. Kratz, A. Mohtashamdolatshahi, D. Eberbeck, O. Kosch, F. Wiekhorst, M. Taupitz, B. Hamm, N. Stolzenburg and J. Schnorr, *Nanomaterials*, 2021, **11**, 1532.
142 X. Z. Violeta and G. Demillo, *Physiol. Behav.*, 2015, **176**, 139–148.
143 S. Liu, A. Chiu-Lam, A. Rivera-Rodriguez, R. DeGroff, S. Savliwala, N. Sarna and C. M. Rinaldi-Ramos, *Nanotheranostics*, 2021, **5**, 348–361.
144 K. Pombo-García, S. Weiss, K. Zarschler, C. S. Ang, R. Hübner, J. Pufe, S. Meister, J. Seidel, J. Pietzsch, L. Spiccia, H. Stephan and B. Graham, *ChemNanoMat*, 2016, **2**, 959–971.
145 S. W. Chou, Y. H. Shau, P. C. Wu, Y. S. Yang, D. Bin Shieh and C. C. Chen, *J. Am. Chem. Soc.*, 2010, **132**, 13270–13278.
146 R. Nasiri, S. Dabagh, R. Meamar, A. Idris, I. Muhammad, M. Irfan and H. Rashidi Nodeh, *Nanotechnology*, 2020, **31**, 195603.
147 A. Villanueva, P. De La Presa, J. M. Alonso, T. Rueda, A. Martínez, P. Crespo, M. P. Morales, M. A. Gonzalez-Fernandez, J. Valdés and G. Rivero, *J. Phys. Chem. C*, 2010, **114**, 1976–1981.
148 J. Lin, W. Zhou, A. Kumbhar, J. Wiemann, J. Fang, E. E. Carpenter and C. J. O'Connor, *J. Solid State Chem.*, 2001, **159**, 26–31.
149 A. J. Wagstaff, S. D. Brown, M. R. Holden, G. E. Craig, J. A. Plumb, R. E. Brown, N. Schreiter, W. Chrzanowski and N. J. Wheate, *Inorg. Chim. Acta*, 2012, **393**, 328–333.
150 S. Kayal and R. V. Ramanujan, *J. Nanosci. Nanotechnol.*, 2010, **10**, 5527–5539.
151 M. Mehdipour, L. Gloag, J. Lian, R. D. Tilley and J. J. Gooding, *Chem. Commun.*, 2021, **57**, 13142–13145.
152 S. Lentijo-Mozo, R. P. Tan, C. Garcia-Marcelot, T. Altantzis, P.-F. Fazzini, T. Hungria, B. Cormary, J. R. Gallagher, J. T. Miller, H. Martinez, S. Schrittwieser, J. Schotter, M. Respaud, S. Bals, G. Van Tendeloo, C. Gatel and K. Soulantica, *ACS Nano*, 2015, **9**, 2792–2804.
153 E. Nassireslami and M. Ajdarzade, *Adv. Pharm. Bull.*, 2018, **8**, 201–209.
154 V. Salgueiriño-Maceira, M. A. Correa-Duarte, M. Farle, A. López-Quintela, K. Sieradzki and R. Diaz, *Chem. Mater.*, 2006, **18**, 2701–2706.
155 M. P. Murphy and H. Levine, *J. Alzheimer's Dis.*, 2010, **19**, 311–323.
156 P. Ludewig, N. Gdaniec, J. Sedlacik, N. D. Forkert, P. Szwargulski, M. Graeser, G. Adam, M. G. Kaul, K. M. Krishnan, R. M. Ferguson, A. P. Khandhar, P. Walczak, J. Fiehler, G. Thomalla, C. Gerloff, T. Knopp and T. Magnus, *ACS Nano*, 2017, **11**, 10480–10488.

157 M. Shilo, A. Sharon, K. Baranes, M. Motiei, J. P. M. Lellouche and R. Popovtzer, *J. Nanobiotechnol.*, 2015, **13**, 1–7.
158 D. E. Markov, H. Boeve, B. Gleich, J. Borgert, A. Antonelli, C. Sfara and M. Magnani, *Phys. Med. Biol.*, 2010, **55**, 6461–6473.
159 G. Song, X. Zheng, Y. Wang, X. Xia, S. Chu and J. Rao, *ACS Nano*, 2019, **13**, 7750–7758.
160 J.-i. Jo, I. Aoki and Y. Tabata, *J. Controlled Release*, 2010, **142**, 465–473.
161 X. Jiang, A. Musyanovych, C. Röcker, K. Landfester, V. Mailänder and G. U. Nienhaus, *Nanoscale*, 2011, **3**, 2028–2035.
162 X. Li, Z. Wei, H. Lv, L. Wu, Y. Cui, H. Yao, J. Li, H. Zhang, B. Yang and J. Jiang, *Int. J. Nanomed.*, 2019, **14**, 573–589.
163 S. Kaushik, J. Thomas, V. Panwar, H. Ali, V. Chopra, A. Sharma, R. Tomar and D. Ghosh, *ACS Appl. Bio Mater.*, 2020, **3**, 779–788.
164 F. Reyes-ortega, Á. V. Delgado and G. R. Iglesias, *Nanomaterials*, 2021, **11**, 1–14.
165 H. M. Joshi, *Bone*, 2011, **23**, 1–7.
166 M. Fantauzzi, F. Secci, M. Sanna Angotzi, C. Passiu, C. Cannas and A. Rossi, *RSC Adv.*, 2019, **9**, 19171–19179.
167 T. Yadavalli, H. Jain, G. Chandrasekharan and R. Chennakesavulu, *AIP Adv.*, 2016, **6**, 055904.